Journal of Medicinal Chemistry

pubs.acs.org/jmc

Drug Annotation

Fragment-Based Discovery of MRTX1719, a Synthetic Lethal Inhibitor of the PRMT5•MTA Complex for the Treatment of *MTAP*-Deleted Cancers

Published as part of the Journal of Medicinal Chemistry special issue "Epigenetics 2022".

Christopher R. Smith,* Ruth Aranda, Thomas P. Bobinski, David M. Briere, Aaron C. Burns, James G. Christensen, Jeffery Clarine, Lars D. Engstrom, Robin J. Gunn, Anthony Ivetac, Ronald Jean-Baptiste, John M. Ketcham, Masakazu Kobayashi, Jon Kuehler, Svitlana Kulyk, J. David Lawson, Krystal Moya, Peter Olson, Lisa Rahbaek, Nicole C. Thomas, Xiaolun Wang, Laura M. Waters, and Matthew A. Marx

Cite This: https://doi.org/10.1021/acs.jmedchem.1c01900

Read Online

ACCESS | Metrics & More | Article Recommendations | Supporting Information

ABSTRACT: The PRMT5•MTA complex has recently emerged as a new synthetically lethal drug target for the treatment of *MTAP*-deleted cancers. Here, we report the discovery of development candidate **MRTX1719**. **MRTX1719** is a potent and selective binder to the PRMT5•MTA complex and selectively inhibits PRMT5 activity in *MTAP*-deleted cells compared to *MTAP*-wild-type cells. Daily oral administration of **MRTX1719** to tumor xenograft-bearing mice demonstrated dose-dependent inhibition of PRMT5-dependent symmetric dimethylarginine protein modification in *MTAP*-deleted tumors that correlated with antitumor activity. A 4-(aminomethyl)phthalazin-1(2*H*)-one hit was identified through a fragment-based screen, followed by X-ray crystallography, to confirm binding to the PRMT5•MTA complex. Fragment growth supported by structural insights from X-ray crystallography coupled with optimization of pharmacokinetic properties aided the discovery of development candidate **MRTX1719**.

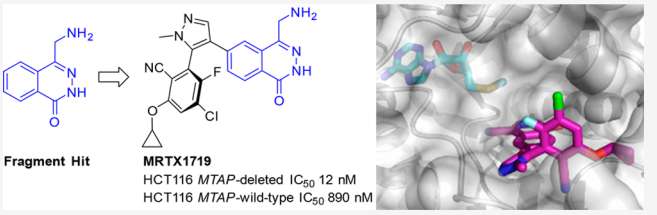

INTRODUCTION

Protein arginine methyltransferase 5 (PRMT5) is a class II PRMT that adds two symmetric methyl groups to arginine residues of its substrate proteins.[1] PRMT5 binds MEP50 (methylosome protein 50) to form a hetero-octameric complex.[2] The PRMT5−MEP50 complex is an integral component of the methylosome[3,4] and methylates a wide range of substrates including spliceosomal Sm proteins, nucleolin, p53, histones H2A, H3, and H4, the SPT5 transcriptional elongation factor, and MBD2.[1,3,5] PRMT5−MEP50 plays an essential role in mammalian cell survival.[6−10] In 2016, multiple independent research teams reported that methylthioadenosine phosphorylase (*MTAP*) gene deletion creates an increased dependency on PRMT5 in *MTAP*-deleted cancers.[11−13] The *MTAP* gene is adjacent to and frequently co-deleted with *CDKN2A*, the most commonly deleted tumor suppressor gene in human cancers. MTAP is required for the methionine salvage pathway, and homozygous gene deletion causes *MTAP*-deleted (*MTAP*-del) cells to accumulate methylthioadenosine (MTA). MTA competes with the activating cofactor *S*-adenosyl-L-methionine (SAM), causing a decrease in PRMT5 activity and sensitizes the *MTAP*-del cells to further loss of PRMT5 activity.[13] This vulnerability has been highlighted as an example of synthetic lethality and has also been referred to as an example of collateral lethality.[4,5] We hypothesized that a compound that preferentially bound to and stabilized the catalytically inactive PRMT5−MEP50•MTA (PRMT5•MTA) complex would inhibit PRMT5 activity in *MTAP*-del tumor cells while preserving PRMT5 activity in *MTAP*-wild-type (*MTAP*-WT) cells, creating a potential precision oncology medicine for the treatment of *MTAP*-deleted cancers.

Several PRMT5 inhibitors, Figure 1, are currently in clinical trials as potential anticancer agents (GSK3326595,[14] JNJ64619178,[15] PF06939999,[16] PRT543,[17] and PRT811).[18] In addition to the clinical compounds, other examples of PRMT5 inhibitors include EPZ015666[19,20] and LLY283.[21] The mechanism of action of the current cohort of clinical PRMT5 inhibitors is either SAM uncompetitive or SAM

Received: November 4, 2021

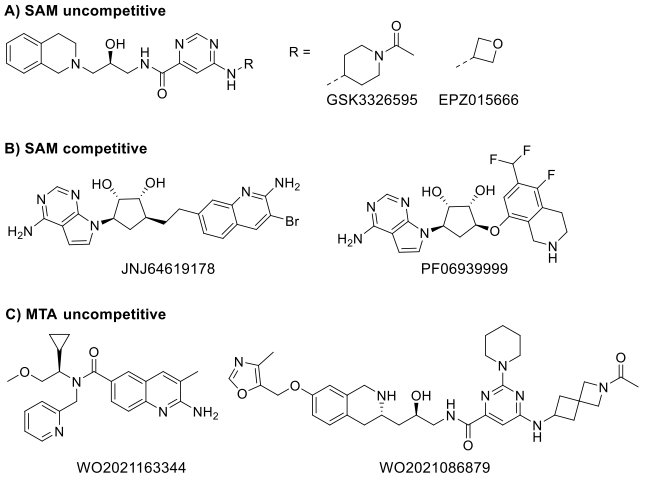

Figure 1. Compound structures of (A) SAM uncompetitive PRMT5 inhibitors GSK3326595 and EPZ015666. (B) SAM competitive PRMT5 inhibitors JNJ64619178 and PF06939999. (C) exemplar MTA uncompetitive PRMT5 inhibitors from patent applications WO2021163344 and WO2021086879.

competitive. They also do not bind to and stabilize the PRMT5•MTA complex. Thus, it is not expected that these agents will selectively inhibit PRMT5 activity in *MTAP*-del tumors. Because of the critical role of PRMT5 as an essential gene in regulating hematopoiesis, the indiscriminate blockade of PRMT5 by non-MTA cooperative inhibitors has been associated with dose-limiting thrombocytopenia, anemia, and neutropenia.[22,23] Thus, the ability to selectively inhibit PRMT5 function in tumor cells while sparing nontumor cells is anticipated to exhibit an improved therapeutic index. Recently published patent applications from two other groups describe compounds that appear to target PRMT5•MTA,[24,25] Figure 1, and a recent poster described compound 1-(4-(methylsulfonyl)benzyl)-*N*-(4-methylthiazol-2-yl)-1*H*-indole-6-carboxamide as a novel MTA noncompetitive PRMT5 inhibitor.[26]

Herein, we report the discovery of development candidate **MRTX1719**. **MRTX1719** is a potent and selective binder to the PRMT5•MTA complex and selectively inhibits PRMT5 activity in *MTAP*-del cells compared to *MTAP*-WT cells. Daily oral administration of **MRTX1719** to tumor xenograft-bearing mice demonstrated dose-dependent inhibition of PRMT5-dependent symmetric dimethylarginine (SDMA) protein modification in *MTAP*-deleted tumors that correlated with antitumor activity. The initial starting point en route to the discovery of **MRTX1719** was a 4-(aminomethyl)phthalazin-1(2*H*)-one fragment hit (**F1**), which was identified through a fragment-based lead discovery (FBLD) approach. Subsequent fragment growth using structure-based drug design (SBDD) enabled the discovery of **MRTX1719** (Figure 2).

RESULTS AND DISCUSSION

Identification and Characterization of Fragment Hits.

FBLD is a lead discovery method that starts with the discovery of low molecular weight hits (roughly 150−300 Da), typically with weak affinity in the range of 10 μM to 1 mM.[27,28] Because of the weak affinity, sensitive biophysical methods are often employed to screen fragment libraries at these high concentrations, including surface plasmon resonance (SPR), ligand- or protein-detected NMR, differential scanning fluorometry (DSF), microscale thermophoresis (MST),[29] biolayer interferometry (BLI),[30] mass spectroscopy, and X-ray protein crystallography. The potency of fragment hits is then increased through fragment growing strategies, often supported by structural insights from X-ray crystallography.[31] Edfeldt et al.[32] described how a combination of hit rates, affinity, and hit diversity derived from a fragment screen can be used to predict ligandability and lead series discovery success for a novel target. We therefore selected an FBLD approach to first assess ligandability of the PRMT5•MTA complex and to then grow and expand around any identified hits. SPR was prioritized as the screening platform due to several anticipated advantages: high sensitivity, ability to detect weak binding, and in combination with a clean screen, the ability to detect nonspecific binding and reduce false positives. Using SPR, we proceeded to screen a commercially available fragment library of 1000 fragments. First, the K_D of MTA was measured with biotinylated PRMT5/MEP50 protein immobilized on a streptavidin sensor-chip (MTA K_D = 661 nM). The PRMT5•MTA complex was then generated on the surface through addition of 20 μM MTA to the running buffer. The EPZ015666 K_D was then determined (K_D = 27 μM), and this compound was used as a positive control. A clean screen identified six nonspecific compounds which were removed from the library, and 994 fragments were screened at a single concentration of 100 μM. Seventeen hits were identified, translating to a preliminary hit rate of 1.7%. These data indicated that a provisional ligandability score for the PRMT5•MTA complex was medium (medium ligandability = intermediate hit rate, best affinities 0.1−1 mM).[32] Interestingly, nine of the 17 hits (approximately 50% of the hits) had a basic center with calculated pK_a ≥ 8, whereas only 22% of the library contained a basic center. This enrichment of basic compounds in the hit set could be expected, for the substrate binding site of PRMT5 includes a pair of acidic glutamate residues (Glu435 and Glu444) known as the "double E loop" and is well suited to recognize basic compounds, including the arginine side chains of its substrates.[33]

Encouraged by the provisional ligandability score, we decided to continue screening fragments by SPR and expand upon the original hit set by screening two additional libraries. These were a diverse library of 1692 fragments and a focused

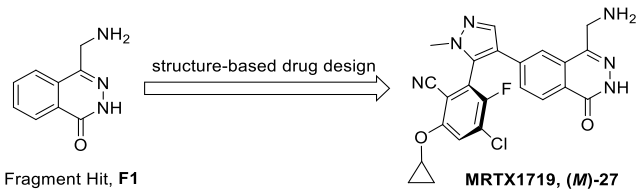

Figure 2. Discovery of development candidate **MRTX1719** from fragment hit **F1** using SBDD and fragment growing strategies.

https://doi.org/10.1021/acs.jmedchem.1c01900
J. Med. Chem. XXXX, XXX, XXX−XXX

library constructed of 194 specifically selected compounds. The objective of the focused library was to identify less-basic hits capable of making productive interactions with the acidic "double E loop". This focused library was built from commercially available fragments with $pK_a \leq 7$, and the selections were made through a combination of ligand and structure-based virtual screens (see Supporting Information).

For the second round of screening, the PRMT5•MTA complex was prepared as previously described, and the two libraries were screened at a single concentration of 500 μM. A total of 188 hits were identified, translating to a preliminary hit rate of 10%. The higher hit rate was presumably due to screening at a 5-fold higher concentration compared to the first screen. The combined hit sets from the three libraries were then progressed to PRMT5•MTA K_D determination to return 100 fragments with saturable K_Ds < 1 mM, representing an overall hit rate of 3.5% (first library seven hits, 0.7%; second library 69 hits, 4%; focused library 24 hits, 12%). Notably, the hit rate for the focused library was significantly higher than for the two diverse libraries. The cumulative screening data including hit rates and K_Ds confirmed the initial ligandability score of medium for the PRMT5•MTA complex.

To determine if the hits bound preferentially to the PRMT5•MTA complex or the PRMT5-MEP50•SAM (PRMT5•SAM) complex, 24 hits with $K_D \leq 500$ μM (F1–F24) were selected for further characterization. The SPR workflow and results are shown in Figure 3. The surface was

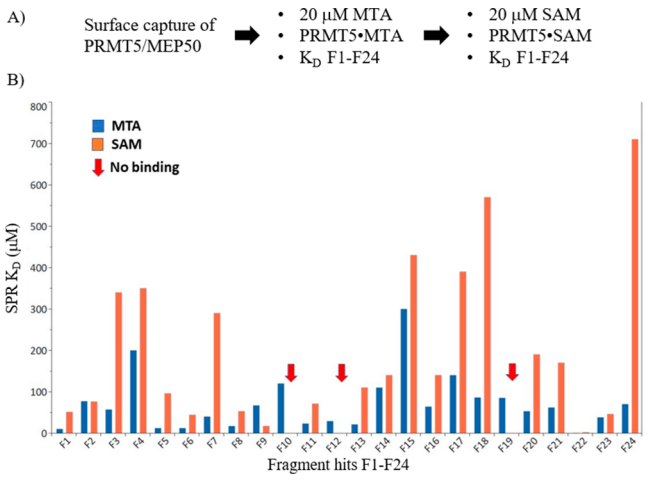

Figure 3. (A) SPR flow scheme designed to determine binding K_D to PRMT5•MTA and PRMT5•SAM in a single run for fragment hits F1–F24. PRMT5–MEP50 was first captured on the chip surface, then 20 μM MTA was added to the running buffer to form the PRMT5•MTA complex and the K_D values determined. MTA was subsequently replaced with 20 μM SAM to form the PRMT5•SAM complex, and the K_D values were again determined for the same set of hits. (B) Binding K_Ds to PRMT5•MTA (blue) and PRMT5•SAM (orange) for fragment hits F1–F24. The red arrows indicate where no binding was observed.

prepared with the capture of PRMT5–MEP50 followed by equilibration with 20 μM MTA in the running buffer to form the PRMT5•MTA complex, and the K_D of positive control EPZ015666 was determined (K_D = 11 μM) to confirm formation of the PRMT5•MTA complex. The fragments were then titrated, followed by a second titration of EPZ015666 (K_D = 13 μM) to confirm surface activity during the run. The MTA in the running buffer was then exchanged for 20 μM SAM to form the PRMT5•SAM complex, and the same 24 fragments were again titrated. At the end of the run, EPZ015666 was titrated, and now the K_D was <1 nM, similar to previously published data, confirming formation of the PRMT5•SAM complex.[19] Because of the slow off-rate kinetics of EPZ015666 binding to the PRMT5•SAM complex, EPZ015666 was run after titrating the fragments and not before, to avoid reduction of surface activity. The K_D of SAM was measured with biotinylated PRMT5–MEP50 protein immobilized on a streptavidin sensor-chip (SAM K_D = 550 nM). Of the 24 fragments tested, binding K_Ds for PRMT5•MTA ranged from 300 nM to 300 μM, with selectivity over the PRMT5•SAM complex ranging from 0.2- to 35-fold as shown in Figure 3. Here we report the data for one of the hits, 4-(aminomethyl)-phthalazin-1(2*H*)-one (**F1**), with PRMT5•MTA K_D = 10 μM and PRMT5•SAM K_D = 51 μM (Table 3).

To understand the binding mode of this novel PRMT5•MTA binder, **F1** was cocrystallized with PRMT5•MTA and PRMT5•SAM. Interestingly, the same X-ray cocrystal structure was obtained for the MTA and SAM conditions, with **F1** bound to the PRMT5•MTA complex. It is known that SAM degrades over time,[34] therefore we hypothesized that SAM was converting to MTA under the conditions of the protein–ligand crystallization protocol, resulting in the formation of PRMT5•MTA•F1 complexes. Figure 4 illustrates the X-ray cocrystal structure of **F1** bound to

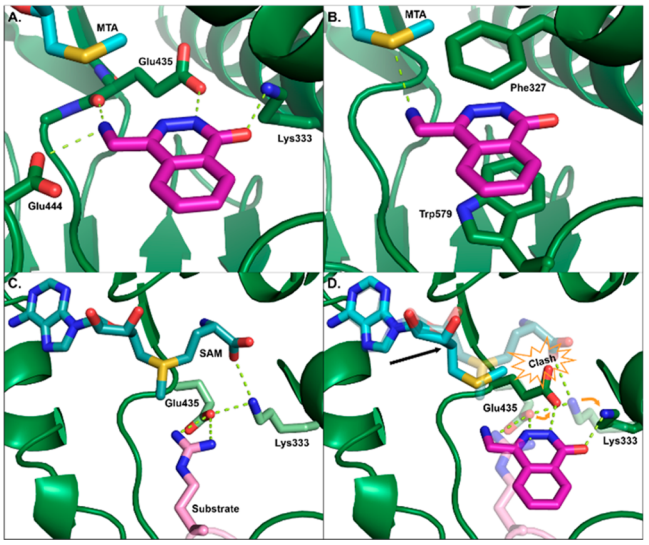

Figure 4. X-ray cocrystal structure of **F1** (magenta) bound to PRMT5•MTA (PDB 7S0U). (A) H-bond interactions with Glu444, Glu435, and Lys333. (B) π-Stack interaction between **F1** and the side chains of Phe327 and Trp579 and van der Waals interaction with the sulfur atom of MTA. (C) PRMT5•SAM H4 peptide cocrystal structure (H4 peptide pink; 4GQB).[2] (D) Overlay of PRMT5•MTA **F1** cocrystal structure with the PRMT5•SAM H4 peptide cocrystal structure, highlighting the new positions of Glu435 and Lys333 side chains with **F1** and the incompatibility with SAM binding.

the PRMT5•MTA complex (PDB 7S0U). The 4-(aminomethyl)phthalazin-1(2*H*)-one fragment binds in the substrate binding site with a series of specific interactions. These include H-bonds between the phthalazine-1(2*H*)-one N–H and the side chain of Glu435 as well as between the phthalazine-1(2*H*)-one carbonyl and side chain of Lys333. In addition, the primary amine of **F1** makes an ionic interaction

https://doi.org/10.1021/acs.jmedchem.1c01900
J. Med. Chem. XXXX, XXX, XXX–XXX

with the Glu444 side chain, an H-bond with the backbone carbonyl of Glu435, and a tight van der Waals interaction with the sulfur atom of MTA. Finally, the aromatic scaffold is sandwiched in a π-stack between the side chains of Phe327 and Trp579. The selectivity of **F1** for the PRMT5•MTA complex can be rationalized by examining the movement of key side chains that are critical for **F1** and SAM binding. **F1** binding causes the Glu435 side chain to move in toward the SAM pocket, setting up a clash between SAM and Glu435. **F1** binding also causes Lys333 to move away from the SAM binding site, breaking a key SAM−Lys333 salt bridge interaction. Thus, the binding mode of **F1** is incompatible with the binding of SAM but accommodates the binding of MTA. As noted above, **F1** makes a tight van der Waals interaction with the divalent sulfur atom of MTA; in contrast, we anticipate **F1** would lose this productive van der Waals interaction with the equivalent trivalent sulfur atom of SAM. This loss of a productive interaction may also contribute to the MTA/SAM selectivity of **F1** binding. Sinefungin is a stabilized analogue of SAM that does not generate MTA under cocrystallization conditions. Indeed, an X-ray costructure of EPZ015666 with PRMT5 and sinefungin bound in the cofactor site was previously reported (PDB 4X60).[19] Therefore, PRMT5 cocrystallization was explored with this "SAM-like" cofactor and **F1**. The experiment returned a PRMT5•sinefungin X-ray cocrystal structure; however, the substrate binding site was unoccupied and no **F1** was present (PDB 7S1P, see the Supporting Information).

Assay Development. We initially envisioned the preferred assays to guide SAR development would be cellular mechanistic and viability assays using isogenic pairs of HCT116 *MTAP*-WT and HCT116 *MTAP*-del cells. HCT116 *MTAP*-WT cells were genetically engineered to knock out the function of both *MTAP* alleles using a CRISPR/Cas9 system in conjunction with an sgRNA targeting the *MTAP* gene (homozygous knockout) to create *MTAP*-del cells. Levels of PRMT5-dependent SDMA protein modification were monitored by an In-Cell Western assay with SYM11 antibody after 96 h of control or test compound incubation in *MTAP*-del and *MTAP*-WT cells. IC_{50} values were determined from nine-point dose−response curves. Cell viability was also monitored at day 10 in *MTAP*-del and *MTAP*-WT cells using the CellTiter-Glo luminescence-based assay. GSK3326595 was used as the positive control with the following IC_{50} values: *MTAP*-del SDMA IC_{50} = 11 nM, *MTAP*-WT SDMA IC_{50} = 12 nM, *MTAP*-del viability IC_{50} = 189 nM, and *MTAP*-WT viability IC_{50} = 237 nM. These data highlight how similar the IC_{50} values are between the *MTAP*-del and *MTAP*-WT cells for a representative PRMT5 inhibitor that is not selective for the PRMT5•MTA complex. However, because of the weak affinity of **F1**, we elected to utilize more sensitive biophysical and radiolabeled biochemical assays for potency determination initially and later transition to cellular assays once affinity had been increased. We selected the FlashPlate PRMT5−MEP50 radiolabeled methyltransferase assay from Reaction Biology Corporation as our primary biochemical assay. To approximate the higher levels of cellular MTA in *MTAP*-del tumor cells, MTA was added to the assay. We hypothesized a compound that preferentially stabilized the PRMT5•MTA complex would show greater inhibition in the presence of MTA. Thus, the IC_{50} of MTA was determined (IC_{50} = 4 μM), and the assay was subsequently run with 2 μM of MTA (MTA+) and without MTA (MTA−). The MTA concentration was selected near its IC_{50} to maintain a window of activity in the assay. One μM of SAM was used in both the MTA+ and MTA− versions of the assay. We anticipated that while this assay would not exactly reflect the *MTAP*-del/*MTAP*-WT selectivity in cellular assays, it could be used as a surrogate for SAR development until the compounds were potent enough to investigate in the cellular assays. EPZ015666 retained activity in the MTA+ assay and was only 2-fold less potent than MTA− (MTA+ IC_{50} = 0.11 μM; MTA− IC_{50} = 0.06 μM). **F1** showed no observable inhibition in the biochemical assay up to 100 μM.

Fragment Growing. Visual inspection of the X-ray cocrystal structure of **F1** and PRMT5•MTA revealed a pocket formed by the residues Leu312, Pro311, Ser310, Gly309, and Val503 that could potentially be accessed by designing substituents vectored off the 6-position of the phthalazinone scaffold. Molecular modeling using MOE[35] indicated that five- and six-membered heterocycles may fit in this pocket and heterocycles with a lone pair pointing toward the backbone N−H of Leu312 may also form a beneficial H-bond interaction. Thus, a series of five- and six-membered heterocycles (compounds **2**−**9**, Table 1) were prepared according to a nine-step synthetic route shown in Scheme 1, starting from 5-bromoisobenzofuran-1(3*H*)-one. Gratifyingly, phenyl analogue **2** was 6-fold more potent than **F1** in the PRMT5•MTA SPR binding assay (K_D = 1.62 μM) and demonstrated inhibition in the biochemical assay (MTA+ IC_{50} = 4.3 μM and MTA− IC_{50} = 14.5 μM). While the potency increase was largely driven by an increase in lipophilicity (ΔcLogP + 1.3), this result confirmed that a six-membered ring would fit in the pocket. Encouraged by this step forward, pyridyl-3-yl analogue **3** was designed so the aromatic nitrogen lone pair would point toward the backbone N−H of Leu312. Indeed, inhibition increased by 5-fold relative to phenyl **2** (MTA+ IC_{50} = 0.91 μM and MTA− IC_{50} = 19.0 μM), while also reducing lipophilicity. Conversely the pyrid-2-yl analogue **4** and pyridazine-3-yl analogue **5** were dramatically less active than **3** with MTA+ IC_{50} = 95.8 μM and MTA+ IC_{50} = 30.1 μM, respectively. A methyl group flanking the pyridyl lone pair of **3**, analogue **6**, was also investigated, but the additional methyl group reduced inhibition by just over 6-fold (MTA+ IC_{50} = 5.8 μM). Several five-membered heterocycles, compounds **7**−**9**, were also investigated. Isothiazol-3-yl analogue **7** (MTA+ IC_{50} = 0.71 μM) had similar potency to **3**, while thiazol-5-yl analogue **8** (MTA+ IC_{50} = 2.85 μM) was 3-fold less potent than **3**. Interestingly, *N*-methylpyrazol-4-yl analogue **9** (MTA+ IC_{50} = 0.30 μM) was 3-fold more potent than 3 and selectivity over the MTA− assay was 19-fold (MTA− IC_{50} = 5.8 μM). Encouraged by this increase in potency and selectivity, the binding parameters K_D, k_{on}, and k_{off} for compound **9** were determined by SPR. Compared to the original fragment **F1**, the addition of the *N*-methylpyrazol-4-yl substituent generated a 2000-fold increase in binding K_D, and selectivity increased from 5-fold to 17-fold (PRMT5•MTA K_D = 5 nM, k_{on} = 1.7 × 10^6 M s^{-1}, k_{off} = 9.2 × 10^{-3}, and PRMT5•SAM K_D = 83 nM, k_{on} = 1.2 × 10^5 M s^{-1}, k_{off} = 9.9 × 10^{-3}, Table 3). Compound **9** PRMT5•MTA SPR K_D is 60-fold more potent than the IC_{50} in the corresponding MTA+ biochemical assay. Presumably, this difference is due to differences in the SPR and biochemical assays. For example, in the biochemical assay, the test compound is in competition with the substrate (histone peptide H4 1−15) and both MTA and SAM are present. In contrast, the SPR assay is detecting binding to the PRMT5•MTA complex with no substrate or

https://doi.org/10.1021/acs.jmedchem.1c01900
J. Med. Chem. XXXX, XXX, XXX−XXX

Table 1. Compounds Designed to Explore the Fragment Growth Vector Off the 6-Position of the Phthalazinone Scaffold

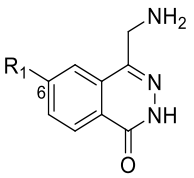

R_1 = grow vector

Cmpd	R_1	PRMT5 biochemical IC_{50} (μM)[a]			MDR1-MDCK A-B (μcm/s)[d] | Efflux ratio
		MTA+[b]	MTA-[c]	MTA-/MTA+ ratio	
F1	H	>100	>100	-	ND
2		4.3	14.5	3	16.0 | 0.8
3		0.91	19.0	21	2.8 | 0.7
4		95.8	>100	-	9.3 | 1.2
5		30.1	>100	-	1.1 | 0.9
6		5.8	69.0	12	4.7 | 3.5
7		0.71	11.6	16	11.1 | 0.8
8		2.85	57.8	220	14.6 | 0.6
9	 logD$_{pH7.4}$ -0.5	0.30	5.8	19	2.3 | 0.6
10		0.51	10.6	21	2.0 | 6.2
11		0.67	11.4	17	1.3 | 20.1
12		0.32	7.65	24	3.2 | 2.7
13		0.71	11.2	16	0.9 | 0.9
14		0.05	1.29	26	4.9 | 0.6

[a]Inhibition of PRMT5 mediated transfer of a tritiated methyl group from *S*-adenosyl-L-[methyl-^{3}H]methionine to a histone 4 peptide (H4 1−15). [b]2 μM MTA. [c]0 μM MTA. All data represent $n \geq 2$. [d]MDCK-MDR1 membrane permeability at 2 μM substrate concentration and pH 7.4.

SAM present. At this stage, compound **9** showed no activity in the cellular assays up to a concentration of 10 μM.

The X-ray cocrystal structure of **9** with PRMT5•MTA (PDB 7S1Q), shown in Figure 5, revealed the initial binding mode of **F1** was maintained. The newly introduced *N*-methylpyrazol-4-yl substituent occupied the pocket formed by Gln309, Ser310, Pro311, Leu312, and Val503 and made a

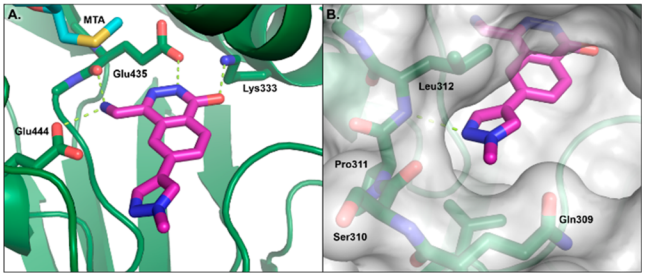

Figure 5. X-ray cocrystal structure of **9** (magenta) bound to PRMT5•MTA. (A) The binding mode of the original fragment is maintained. (B) The *N*-methylpyrazol-4-yl substituent occupies a pocket formed by Gln309, Ser310, Pro311, and Leu312 and makes a productive H-bond interaction with the Leu312 backbone N−H.

favorable H-bond interaction with the Leu312 backbone N−H. A series of analogues with larger pyrazole *N*-1 substituents were investigated (compounds **10**−**13**, -ethyl, -propyl, -isopropyl, and -hydroxyethyl, respectively, Table 1). These compounds maintained MTA+ IC_{50} within 3-fold of **9** but did not substantially increase inhibition. Presumably, this was because the substituents were oriented toward the front of the pocket and into a highly solvent-exposed region. Conversely, addition of a methyl group to C5 of the *N*-methylpyrazol-4-yl group (compound **14**) resulted in a 10-fold boost in inhibition compared to **9** with 26-fold selectivity (MTA+ IC_{50} = 0.05 μM and MTA− IC_{50} = 1.29 μM).

At this point, the membrane permeability of compounds **2**−**14** was assessed in a Madin−Darby Canine Kidney cell transwell permeability assay transfected with multidrug resistance gene-1 (MDCK-MDR1). Apical to basal (A−B) and basal to apical (B−A) rates were measured (P_{app} μcm/s) and efflux ratios calculated. Overall, the permeability of compounds in Table 1 was in the low to moderate range with efflux ratios <4, except for **10** and **11**, having efflux ratios 6.2 and 20.1, respectively, Table 1.

Analysis of the ratio between the MTA+ and MTA− IC_{50}s for compounds **3**−**14** revealed the conditional selectivity ratio was in a tight range between 12-fold and 26-fold. Therefore, we focused on the MTA+ assay alone to drive understanding of SAR for the next set of analogues. Encouraged by the potency of compound **14**, further exploration of the C5 vector from the *N*-methylpyrazol-4-yl group was investigated. Examination of the X-ray cocrystal structure of **9** (Figure 6) identified that a lipophilic pocket created by the side chains of

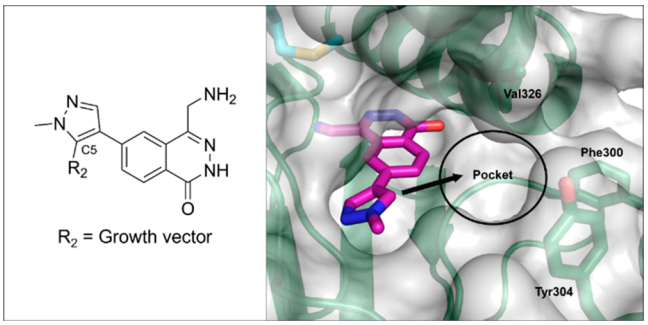

Figure 6. Structure-based rationale for designing compounds growing off the C5 *N*-methylpyrazol-4-yl vector. C5 is a well-oriented vector to add substituents to explore the lipophilic pocket created by the side chains of Tyr304, Val326, and Phe300.

https://doi.org/10.1021/acs.jmedchem.1c01900
J. Med. Chem. XXXX, XXX, XXX−XXX

Table 2. Characterization of Biochemical Potency, Cellular Activity, and in Vitro ADMET Properties of Compounds 9 and 15−31

Compound	R_2 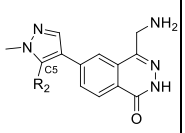	PRMT5 IC_{50} MTA+ (nM)[a]	SDMA IC_{50} HCT116 *MTAP*-del | *MTAP*-WT (nM)[b]	Viability IC_{50} HCT116 *MTAP*-del | *MTAP*-WT (nM)[c]	H | Ms hep Cl_{int} mL/min/Kg[d]	MDCK A-B (μcm/s)[e] | efflux ratio
9	H	300	-	-	-	23 | 0.6
15	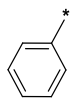	3	2,470 | 9,810	3,652 | 4,060	23 | 123	1.5 | 20
16	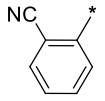 $logD_{pH7.4}$ 0.2	4	826 | 3,165	5,230 | >10,000	<18 | 148	1.6 | 7.0
17	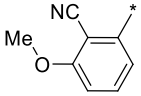	1	62 | >10,000	851 | >10,000	<18 | 137	0.6 | 20
18	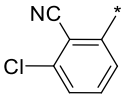	2	62 | 8,811	544 | >10,000	<18 | 232	0.7 | 35
19	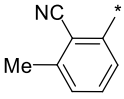	3	101 | 8,830	365 | >10,000	29 | 296	0.6 | 36
20	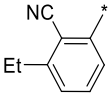	2	79 | 3,210	175 | >10,000	18 | 523	0.3 | 35
21	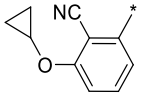	1	34 | 6,550	129 | 6,820	<18 | 237	0.3 | 104
22	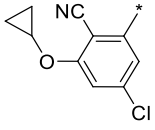	-	8 | 834	41 | 990	<18 | 336	0.2 | 121
23	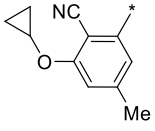	-	9 | -	77 | 1,290	21 | 175	0.4 | 62
24	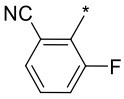	4	322 | >10,000	761 | 7,440	18 | 171	0.3 | 42
25	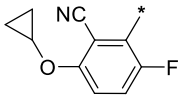	-	16 | -	43 | 2,176	18 | 143	0.2 | 143
(*M*)-25	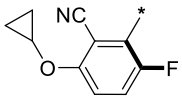	-	4 | 1,055	17 | 3,620	<18 | 87	0.2 | 123

https://doi.org/10.1021/acs.jmedchem.1c01900
J. Med. Chem. XXXX, XXX, XXX−XXX

Table 2. continued

Compound	R_2	PRMT5 IC_{50} MTA+ (nM)[a]	SDMA IC_{50} HCT116 *MTAP*-del | *MTAP*-WT (nM)[b]	Viability IC_{50} HCT116 *MTAP*-del | *MTAP*-WT (nM)[c]	H | Ms hep Cl_{int} mL/min/Kg[d]	MDCK A-B (μcm/s)[e] | efflux ratio
(*P*)-25	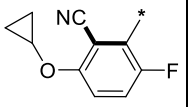	-	65 | 4,483	112 | 4,214	- | -	0.2 | 150
26	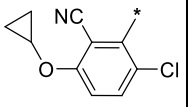	-	11 | >1,000	91 | 1,646	<18 | 332	0.3 | 131
27	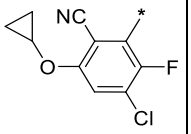	-	6 | -	41 | -	-	<0.2 | >252
MRTX1719 (*M*)-27	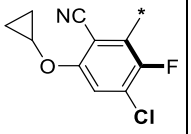 $logD_{pH7.4}$ 0.2; pka 8.0	-	8 | 653	12 | 890	<18 | 253	<0.2 | >203
(*P*)-27	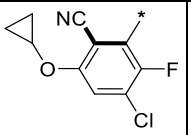	-	1,520 | >5,500	3,470 | >10,000	<18 | 316	0.3 | 116
28	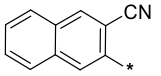	-	118 | -	264 | 5,090	<18 | 212	0.5 | 31
29	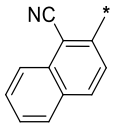	-	11 | 1,210	49 | 1,976	<18 | 340	0.4 | 99
30	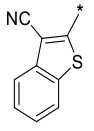	-	5 | >1,000	58 | 5,800	41 | 280	0.6 | 58
(*M*)-31	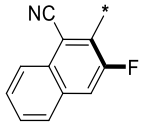	-	3 | 569	10 | 1,020	18 | 255	0.4 | 85
(*P*)-31	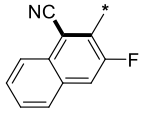	-	70 | >1,000	210 | 5,930	<18 | 293	0.3 | 136

[a]Inhibition of PRMT5 mediated transfer of a tritiated methyl group from *S*-adenosyl-L-[methyl-3*H*]methionine to a histone 4 peptide (H4 1−15) with 2 μM MTA. [b]Inhibition of SDMA assessed at 96 h by in-cell Western in HCT116 *MTAP*-del and *MTAP*-WT cells. [c]Inhibition of viability evaluated on day 10 by the CellTiter-Glo luminescence-based assay in HCT116 *MTAP*-del and *MTAP*-WT cells. All data represent $n \geq 2$. [d]Intrinsic clearance obtained from scaling in vitro half-lives from pooled hepatocytes. [e]MDCK-MDR1 membrane permeability at 2 μM substrate concentration and pH 7.4.

Phe300, Tyr304, and Val326 could be reached with substituents vectored off the C5 position of the *N*-methylpyrazol-4-yl group. The partition coefficient between water and octanol at pH 7.4 (Log $D_{pH7.4}$) was also measured for compound **9** (Log $D_{pH7.4}$ = −0.5). This relatively high polarity for an oral drug was viewed as an opportunity to add lipophilicity to this C5 vector. We targeted Log $D_{pH7.4}$ values in the 1−3 range guided by an analysis of the literature on physicochemical properties of optimized orally available compounds.[36−39] Indeed, addition of the lipophilic phenyl

https://doi.org/10.1021/acs.jmedchem.1c01900
J. Med. Chem. XXXX, XXX, XXX−XXX

group gave compound **15** (MTA+ IC_{50} = 3 nM, Table 2), a 100-fold increase in potency compared to compound **9**. This increase in biochemical potency translated to modest activity in the cellular assays: *MTAP*-del SDMA IC_{50} = 2.47 μM, *MTAP*-WT SDMA IC_{50} = 9.81 μM, *MTAP*-del viability IC_{50} = 3.65 μM, and *MTAP*-WT viability IC_{50} = 4.06 μM. Gratifyingly, the addition of a 2-nitrile substituent to the phenyl group to give compound **16** resulted in a sub-μM IC_{50} in the *MTAP*-del SDMA assay with 4-fold selectivity over the respective *MTAP*-WT assay (*MTAP*-del SDMA IC_{50} = 0.83 μM and *MTAP*-WT SDMA IC_{50} = 3.17 μM). In the viability assay, the IC_{50} of compound **16** was 5.23 μM in *MTAP*-del cells and >10.0 μM in *MTAP*-WT. Compound **16** provided the first proof-of-concept that selectivity between *MTAP*-del and *MTAP*-WT cells could be achieved in this series.

Several analogues of **16** were designed to probe a small lipophilic pocket sandwiched between Phe300 and Tyr304. Small, lipophilic substituents ortho to the nitrile group, −methoxy (**17**), −chloro (**18**), −methyl (**19**), −ethyl (**20**), and −cyclopropoxyl (**21**) were synthesized and tested, Table 2. These compounds were at the lower limit of detection in the MTA+ enzymatic assay (IC_{50} ∼ 1−3 nM); therefore, we transitioned to the *MTAP*-del and *MTAP*-WT cellular assays to continue the SAR exploration. Each analogue improved SDMA IC_{50} in *MTAP*-del cells compared to **16** and maintained selectivity over *MTAP*-WT cells in this assay, as shown in Table 2. This improvement in *MTAP*-del SDMA inhibition also translated to inhibition of viability in *MTAP*-del cells with excellent selectivity over *MTAP*-WT viability. For example, compound **21**: *MTAP*-del SDMA IC_{50} = 34 nM, *MTAP*-WT SDMA IC_{50} = 6.55 μM (193-fold selectivity), *MTAP*-del viability IC_{50} = 129 nM, and *MTAP*-WT viability IC_{50} = 6.82 μM (53-fold selectivity). These results provided convincing evidence that the phthalazinone series could achieve potent and selective inhibition of viability in *MTAP*-del cells compared to *MTAP*-WT cells, suggesting that in vivo antitumor efficacy may also be achieved by this approach.

The in vitro intrinsic clearance (Cl_{int}) parameters were measured in human and mouse hepatocytes with the goal to identify a compound with low human intrinsic clearance defined by the following criteria: low human $Cl_{int} \leq 20$ mL/min/kg and moderate to high human $Cl_{int} > 20$ mL/min/kg. Compounds **16**, **17**, **18**, **20**, and **21** demonstrated promising low human intrinsic clearance, while **19** was in the moderate to high range. The MDCK permeability was also measured, and compounds **15**−**21** had A−B values in the range 0.3−1.6 μcm/s and efflux ratios in the range 7−104. To understand the translation of in vitro ADME properties to in vivo characteristics of lead compounds, the pharmacokinetic (PK) properties of **18** were evaluated in CD-1 mice as shown in Table 4. Following a 3 mg/kg IV dose of compound **18** to CD-mice (n = 3), clearance was 121 mL/min/kg, volume of distribution was 6.6 L/kg, and half-life was 1.3 h. Oral administration of a 30 mg/kg dose of **18** to mice (n = 3) resulted in a C_{max} of 0.22 μg/mL and AUC_{inf} of 0.49 h•μg/mL, with 13% bioavailability. Although the clearance of **18** was above mouse liver blood flow of 90 mL/min/kg, the oral bioavailability of 13% indicated the compound was orally absorbed. This observation was encouraging for, despite the high efflux ratio of 35, compound **18** was orally absorbed, presumably saturating efflux transporters at the 30 mg/kg dose.

Additional SAR studies around the 2-cyclopropoxy-6-yl-benzonitrile group of **21** focused on probing potential van der Waals interactions between the side chain of residues Leu312, Thr323, and Val326 and small lipophilic substituents −fluoro, −chloro, and −methyl (analogues **22**−**24**, Table 2). The addition of a 4-chloro substituent to give 2-cyclopropoxy-4-chloro-6-yl-benzonitrile analogue **22** (*MTAP*-del viability IC_{50} = 41 nM) increased potency 3-fold in the *MTAP*-del viability assay compared to **21** with 24-fold selectivity over the corresponding *MTAP*-WT viability assay. Similarly, 2-cyclopropoxy-4-methyl-6-yl-benzonitrile analogue **23** incorporating a 4-methyl substituent (*MTAP*-del viability IC_{50} = 77 nM) increased cellular potency approximately 2-fold in the *MTAP*-del viability assay compared to **21**. Guided by the observation that 5-fluoro-6-yl-benzonitrile compound **24** (*MTAP*-del viability IC_{50} = 761 nM) enhanced cellular inhibition compared to the nonfluorinated analogue **16** (*MTAP*-del viability IC_{50} = 5,239 nM), 2-cyclopropoxy-5-fluoro-6-yl-benzonitrile analogue **25** was designed. Indeed, addition of the 5-fluoro substituent increased potency 3-fold in the *MTAP*-del viability assay (*MTAP*-del viability IC_{50} = 43 nM) compared to **21** while maintaining an approximate 50-fold ratio in the corresponding *MTAP*-WT assay. Interestingly, 2-cyclopropoxy-5-chloro-6-yl-benzonitrile analogue **26** was less potent in the *MTAP*-del viability assay (*MTAP*-del viability IC_{50} = 91 nM). Presumably the larger 5-chloro substituent creates a clash with the side chain of Leu312. The SAR for analogues **22** and **25** was then combined to give 2-cyclopropoxy-4-chloro-5-fluoro-6-yl-benzonitrile, compound **27** (*MTAP*-del viability IC_{50} = 41 nM), which had the same IC_{50} in the *MTAP*-del viability assay as **22** and **25**.

Analysis of the ^{1}H NMR spectra of the three potent compounds, **22**, **25**, and **27**, revealed the methylene H_A−H_B signals of the $-CH_2NH_2$ group were multiplets, indicating the possible presence of slowly interconverting rotational isomers. To further investigate, the rotational energy barrier (ΔE_{rot}) of the biaryl bond between the 2-cyclopropoxy-6-yl-benzonitrile and *N*-methylpyrazole groups was calculated for each using quantum mechanical calculations and Spartan18 software,[40] as described by LaPlante et al.[41,42] The ΔE_{rot} values and provisional atropisomer classification were: compound **22**, 24.8 kcal/mol, class 2, compound **25**, 31.2 kcal/mol, class 3, and compound **27**, 31.5 kcal/mol, class 3. Our objective was to identify a lead compound that could be developed as a single compound from either class 1 (free rotation) or class 3 (slow to no rotation) and avoid class 2 atropisomerism (interconversion half-life ∼ hours−days) and the associated potential complications in development for this class.[41] Attempts to separate the atropisomers of **22** by chiral supercritical fluid chromatography (SFC) were not successful, and this compound was not progressed further. The more sterically congested compound **27**, with the higher ΔE_{rot}, was successfully separated by SFC to give atropisomers (***M***)-**27** (**MRTX1719**) and (***P***)-**27**. The cellular potency of the eutomer **MRTX1719** in the *MTAP*-del SDMA assay was IC_{50} = 8 nM and in the *MTAP*-del viability IC_{50} = 12 nM, with 82-fold and 74-fold selectivity to the corresponding *MTAP*-WT assays. The distomer (***P***)-**27** was notably less active with IC_{50} = 1.52 μM in *MTAP*-del SDMA assay and IC_{50} = 3.47 μM in the *MTAP*-del viability assay. A provisional assignment of the stereochemistry was made based on molecular modeling and according to the helical analogy *M* (minus) or *P* (plus) for the naming of atropisomers.[43] The X-ray cocrystal structure of **MRTX1719** with PRMT5•MTA (PDB 7S1S, Figure 7), revealed **MRTX1719** adopted a binding mode in which the 4-

https://doi.org/10.1021/acs.jmedchem.1c01900
J. Med. Chem. XXXX, XXX, XXX−XXX

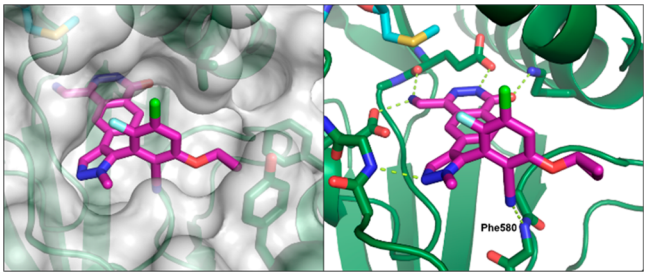

Figure 7. X-ray cocrystal structure of **MRTX1719** (magenta) bound to PRMT5•MTA (PDB 7S1S). Aryl nitrile makes a favorable H-bond interaction with Phe580 backbone N−H and confirms assignment of the rotational isomer stereochemistry.

(aminomethyl)-6-(1-methyl-1*H*-pyrazol-4-yl)phthalazin-1(2*H*)-one substructure overlaid well with compound **9**, and the additional 2-cyclopropoxy-4-chloro-5-fluoro-6-yl-benzonitrile group was oriented perpendicular to the *N*-methylpyrazole group. The fluoro substituent pointed toward Leu312, and the nitrile made a favorable H-bond with the Phe580 backbone N−H. This X-ray cocrystal structure confirmed the provisional assignment of stereochemistry. The structure also provided a rationale for why the (*P*)-atropisomer was less active. In a model of (***P***)-**27**, where the 4-(aminomethyl)-6-(1-methyl-1*H*-pyrazol-4-yl)phthalazin-1(2*H*)-one substructure maintains its binding mode and the opposite rotational isomer is modeled, the nitrile would clash with the Leu312 side chain and the fluoro substituent pointing toward the Phe580 backbone N−H would not make a productive H-bond. In vitro ADME profiling showed the human hepatocyte intrinsic clearance of **MRTX1719** was <18 mL/min/kg and the mouse hepatocyte Cl_{int} = 253 mL/min/kg. The MDCK permeability was low with a high efflux ratio (P_{app} A−B < 0.2 μcm/s and efflux ratio >203).

Encouraged by the ability to successfully separate the rotational isomers of **27**, the same SFC method was used to successfully separate the atropisomers of **25**. The cell potency of the eutomer (***M***)-**25** in the *MTAP*-del SDMA assay was IC_{50} = 4 nM and in the *MTAP*-del viability IC_{50} = 17 nM, with 263-fold and 213-fold selectivity to the corresponding *MTAP*-WT assays. The distomer (***P***)-**25**, was again notably less active, with IC_{50} = 65 nM in the *MTAP*-del SDMA assay and IC_{50} = 112 nM in the *MTAP*-del viability assay.

An alternative approach exploring the SAR around compound **16** was also investigated, and this focused on lipophilic bicyclic groups as alternatives to the monocyclic 2-cyclopropoxy-6-yl-benzonitrile system. Therefore, bicyclic cyano-substituted naphthyl and benzothiophene analogues **28**−**30** were investigated, Table 2. 2-cyano-naphth-3-yl analogue **28** (*MTAP*-del SDMA IC_{50} = 118 nM and *MTAP*-del viability IC_{50} = 264 nM) was less potent than **21**, whereas cyanonaphth-2-yl analogue **29** (*MTAP*-del SDMA IC_{50} = 11 nM and *MTAP*-del viability IC_{50} = 49 nM) and 3-cyano-benzo[*b*]thiophen-2-yl analogue **30** (*MTAP*-del SDMA IC_{50} = 5 nM and *MTAP*-del viability IC_{50} = 58 nM) were more potent than **21**. The X-ray cocrystal structures of compounds **29** and **30** with PRMT5•MTA (PDBs 7SES and 7SER), revealed that both compounds adopted a similar binding mode to **MRTX1719**, with the cyano group in each case making a productive H-bond interaction with Phe580, and no significant changes were observed in the protein and ligand conformations (see Supporting Information).

In a similar fashion to what was previously described, the ΔE_{rot} of the biaryl bonds between the bicyclic-nitrile and *N*-methylpyrazole groups of **29** and **30** were calculated and a provisional classification of the atropisomer class made: compound **29**, 25.4 kcal/mol, class 2, and compound **30**, 12.3 kcal/mol, class 1. After assessing up to 70 chiral SFC and HPLC conditions, efforts to separate the atropisomers of **29** were abandoned and **29** was not progressed further. The class 1 designation for compound **30** was confirmed by analysis of the ^{1}H NMR spectrum of **30**, which revealed the methylene H_A−H_B signal of −CH_2NH_2 was a singlet under a range of ^{1}H NMR conditions (CD_3OD @ 25 °C, $C_2D_2Cl_4$ @ 0 °C, and Py-D5 @ 0 °C, see Supporting Information for spectra), thus confirming fast rotation about the biaryl bond. Compound **30** was our first example of a class 1 compound with sub-100 nM IC_{50} in the *MTAP*-del viability assay from this series. The class 1, freely interconverting rotational properties of **30**, were of interest; however, the human hepatocyte intrinsic clearance was high (Cl_{int} = 41 mL/min/kg), and **30** was less potent than **MRTX1719**. Compound **30** was therefore not progressed further, and additional investigation of the SAR for the 3-cyano-benzo[*b*]thiophen-2-yl series, not reported here, did not identify a class 1 atropisomeric compound with similar or better overall properties than **MRTX1719**.

Inspired by the potency of **MRTX1719**, a similar fluorine substituent was added to **29**, which resulted in the identification of separable atropisomers (***M***)-**31** and (***P***)-**31**. (***M***)-**31** was revealed as the eutomer (*MTAP*-del SDMA IC_{50} =

Table 3. Binding Characterization of Fragment Hit F1, Compound 9, and MRTX1719 to PRMT5•MTA and PRMT5•SAM by SPR

compd	cofactor 20 μM	k_{on} M s^{-1}	k_{off} s^{-1}	K_D	ratio
F1	MTA			10 μM[a]	5×
	SAM			51 μM[a]	
9	MTA	1.7×10^6	9.2×10^{-3}	5 nM[a]	17×
	SAM	1.2×10^5	9.9×10^{-3}	83 nM[a]	
	no cofactor			110 μM[b]	
MRTX-1719	MTA	4.0×10^6	5.8×10^{-7}	0.14 pM[c]	67×
	SAM	2.0×10^5	1.9×10^{-6}	9.4 pM[c]	

[a]PRMT5/MEP50 7-point SPR assay with preincubation with 20 μM MTA or 20 μM SAM. [b]PRMT5/MEP50 5-point SPR assay with no cofactor. [c]PRMT5/MEP50 4-point SPR assay run in chaser mode to determine k_{off} with 20 μM MTA or 20 μM SAM preincubation. k_{off} determined as the average of 3 chaser molecules. All data represent $n \geq 2$.

https://doi.org/10.1021/acs.jmedchem.1c01900
J. Med. Chem. XXXX, XXX, XXX−XXX

Table 4. PK Characterization of Compounds 18, MRTX1719, and (*M*)-31

compd	mouse	dog	cynomolgus monkey
	Cl_{total} (mL/min/kg) | Vd_{ss} (L/kg) | $t_{1/2}$ (h) | *F* (%)[a]	Cl_{total} (mL/min/kg) | V_{ss} (L/kg) | $t_{1/2}$ (h) | *F* (%)[b]	Cl_{total} (mL/min/kg) | V_{ss} (L/kg) | $t_{1/2}$ (h) | *F* (%)[c]
18	121 | 6.6 | 1.3 | 12		
MRTX-1719	83 | 6.3 | 1.5 | 80	14 | 3.4 | 4.8 | 59	15 | 2.3 | 6.1 | 41
(*M*)-**31**	78 | 5.3 | 1.5 | 34	21 | 4.4 | 3.9 | 60	24 | 3.3 | 2.6 | 28

[a]IV/PO dosing in CD-1 mouse (vehicle, IV: 3 mg/kg, 20% SBE-β-CD in 50 mM citric acid pH 5; PO: 30 mg/kg, 0.5% MC (4000 cps)/0.2% Tween 80 in water). [b]IV/PO dosing beagle dog (vehicle, IV: 2 mg/kg, 20% SBE-β-CD in 50 mM citric acid pH 5; PO: 10 mg/kg, 0.5% MC (4000 cps)/0.2% Tween 80 in water). [c]IV/PO dosing in cynomolgus monkey (vehicle, IV: 2 mg/kg, 20% SBE-β-CD in 50 mM citric acid pH 5; PO: 10 mg/kg, 0.5% MC (4000 cps)/0.2% Tween 80 in water).

3 nM, *MTAP*-del viability IC_{50} = 10 nM, *MTAP*-WT SDMA IC_{50} = 569 nM, and *MTAP*-WT viability IC_{50} = 1020 nM), and the stereochemistry of the atropisomer was again confirmed by an X-ray cocrystal structure of (*M*)-**31** with PRMT5•MTA (PDB 7S1R, see Supporting Information). The distomer (*P*)-**31** was less potent (*MTAP*-del SDMA IC_{50} = 70 nM and *MTAP*-del viability IC_{50} = 210 nM). The intrinsic clearance in human hepatocytes for (*M*)-**31** was low (Cl_{int} = 18 mL/min/kg), and the MDCK permeability was low with a high efflux ratio (P_{app} A−B = 0.4 μcm/s and efflux ratio = 85). Despite the low permeability and high efflux ratio in the MDCK assay and on account of the encouraging oral absorption observed for compound **18**, both **MRTX1719** and (*M*)-**31** were advanced to in vivo PK studies.

Biophysical Characterization. The binding kinetics and PRMT5•MTA/PRMT5•SAM selectivity were determined for **MRTX1719** using SPR (Table 3). Indeed, **MRTX1719** is an extremely potent binder to the PRMT5•MTA complex, with K_D = 0.140 pM and a long dissociation half-life: k_{off} half-life = 14 days. **MRTX1719** binds 67-fold less potently to PRMT5•SAM, with K_D = 9.4 pM and with a shorter half-life: k_{off} half-life = 4.6 days. Direct observation of compound dissociation from the PRMT5•MTA and PRMT5•SAM surfaces suffered intrinsic signal drift due to their long dissociation half-lives, therefore, to generate these data, a chaser SPR assay[44] was developed to determine the kinetic binding parameters. The PRMT5•MTA and PRMT5•SAM binding sites were each in turn fully occupied with **MRTX1719**. Subsequently, a competitive chaser molecule was added to the running buffer at various time points up to 56 h in the MTA experiment and up to 20 h in the SAM experiment. As **MRTX1719** dissociated from the protein, the binding signal of the chaser molecule increased. Examination of the kinetic k_{on} and k_{off} parameters revealed that the increase in potency from compound **9** to **MRTX1719** was primarily driven by a 10 000-fold decrease in off-rate. **9** k_{off} = 9.2 × 10^{-3} s^{-1} and **MRTX1719** k_{off} = 5.8 × 10^{-7} s^{-1}, while the on-rates remained similar, 1.7 × 10^6 and 4.0 × 10^6 M s^{-1} respectively. The PRMT5•MTA/PRMT5•SAM selectivity was driven by a combination of a faster on-rate and a slower off-rate for **MRTX1719** in the MTA versus SAM conditions. Additional description of the chaser SPR experiment is available in the Supporting Information. The 67-fold selectivity observed in the PRMT5 binding experiments between the MTA and SAM conditions correlated well with the selectivity observed in the HCT116 *MTAP*-del and HCT116 *MTAP*-WT cell assays with SDMA selectivity = 82-fold and viability selectivity = 74-fold. The shift in the PRMT5•MTA SPR derived K_D to the cellular IC_{50} in the SDMA HCT116 *MTAP*-del assay is notable at 57,142-fold. Presumably, this is driven in part by differences between the SPR and cellular experiments. For SPR, the PRMT5−MEP50 protein is isolated on a surface and ligand binding is detected. Whereas, for the SDMA cell assay, the PRMT5−MEP50 protein in its native state as a hetero-octameric complex along with substrate adaptor proteins Riok1 and pICIn[2] and a functional end point is evaluated.

The activity of **MRTX1719** was examined across a panel of 42 methyltransferase enzymes. In summary, IC_{50} values were >10 μM except for PRMT5−MEP50 IC_{50} = 410 nM and PRMT5(C449S)−MEP50 (IC_{50} = 717 nM) (see Supporting Information for additional details).

PK Profiling in Preclinical Species. The PK properties of **MRTX1719** and (*M*)-**31** were evaluated in CD-1 mice and beagle dogs (Table 4). Following a 3 mg/kg IV dose of compound **MRTX1719** to CD-1 mice (n = 3), clearance was 83 mL/min/kg, volume of distribution was 6.3 L/kg, and half-life was 1.5 h. Oral administration of a 30 mg/kg dose of **MRTX1719** to mice (n = 3) resulted in a C_{max} of 1.16 μg/mL, and AUC_{inf} of 4.85 h•μg/mL, with 80% oral bioavailability. Following a 2 mg/kg IV dose of compound **MRTX1719** to beagle dogs (n = 3), clearance was 14 mL/min/kg, volume of distribution was 3.4 L/kg, and half-life was 4.8 h. Oral administration of a 10 mg/kg dose of **MRTX1719** to beagle dogs (n = 3) resulted in a C_{max} of 1.40 μg/mL, and AUC_{inf} of 7.47 h•μg/mL, with 59% oral bioavailability. Following a 3 mg/kg IV dose of compound (*M*)-**31** to CD-1 mice (n = 3), clearance was 78 mL/min/kg, volume of distribution was 5.3 L/kg, and half-life was 1.5 h. Oral administration of a 30 mg/kg dose of (*M*)-**31** to mice (n = 3) resulted in a C_{max} of 0.59 μg/mL, and AUC_{inf} of 2.73 h•μg/mL, with 34% oral bioavailability. Then, following a 2 mg/kg IV dose of compound (*M*)-**31** to beagle dogs (n = 3), clearance was 21 mL/min/kg, volume of distribution was 4.4 L/kg, and half-life was 3.9 h. Oral administration of a 10 mg/kg dose of (*M*)-**31** to beagle dogs (n = 3) resulted in a C_{max} of 0.88 μg/mL and AUC_{inf} of 4.80 h•μg/mL with 60% oral bioavailability. The PK profiles of **MRTX1719** and (*M*)-**31** in mice and dogs were similar, with **MRTX1719** showing a higher oral bioavailability in mice. To further explore differences in preclinical PK profiles between **MRTX1719** and (*M*)-**31**, the IV and PO PK properties were investigated in cynomolgus monkeys. The data are shown in Table 4 and highlights that **MRTX1719**, when compared to (*M*)-**31**, has a lower clearance (15 mL/min/kg versus 24 mL/min/kg), longer IV half-life (6.1 h versus 2.6 h), and higher oral bioavailability (41% versus 28%). Thus, **MRTX1719** was selected for further characterization and in vivo efficacy studies.

MRTX1719 Displays PD and Efficacy in an *MTAP*-del Mouse Xenograft Efficacy Model of Lung Cancer. **MRTX1719** was investigated in a nude mouse xenograft

https://doi.org/10.1021/acs.jmedchem.1c01900
J. Med. Chem. XXXX, XXX, XXX−XXX

efficacy model employing Lu-99 tumor cells. Lu-99 is an *MTAP*/*CDKN2A*-deleted human lung cancer cell line. When tumors reached ~200 mm^3, **MRTX1719** was dosed once daily via oral gavage (12.5, 25, 50, and 100 mg/kg) until day 21. Tumor volume was measured throughout the study, and PRMT5-meditated SDMA protein modification in tumors was measured using the SYM11 antidimethyl arginine antibody on day 21. Plasma drug concentrations on day 21 at 4 h were also measured. Tumor growth inhibition (TGI) was observed in a dose-dependent manner, with 86% TGI at 50 mg/kg and 88% TGI at 100 mg/kg QD (Figure 8). A reduction in PRMT5-

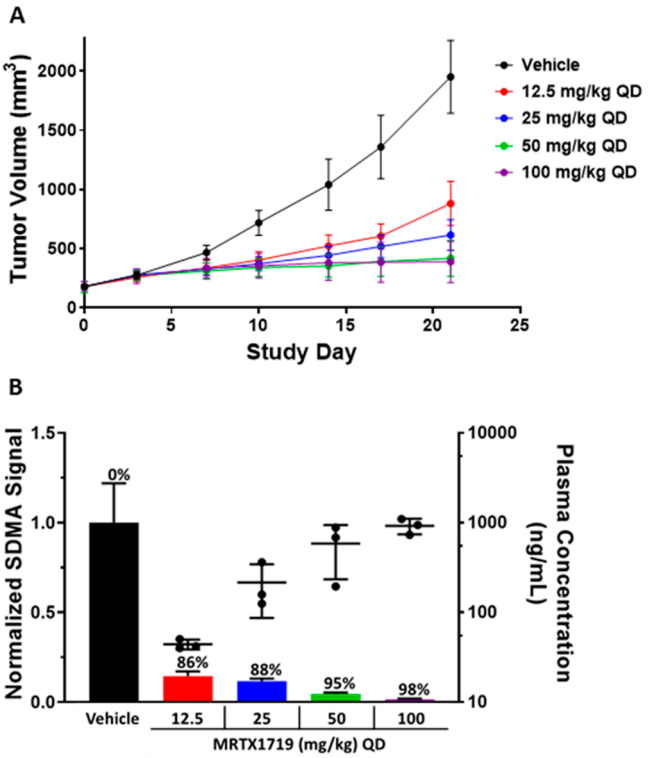

Figure 8. Mouse xenograft efficacy model employing Lu-99 human tumor cells. (A) TGI curves with **MRTX1719** dosed at 12.5, 25, 50, and 100 mg/kg for 21 days. (B) Inhibition of tumor SDMA signal and **MRTX1719** plasma concentrations at 4 h across the dose range.

mediated SDMA levels, 86–98% inhibition, was also observed relative to control, and the plasma concentrations of **MRTX1719** at 4 h increased in a dose-dependent manner. Drug treatment was well tolerated, with no or minimal body weight loss across the dose ranges tested. These data demonstrate concentration- and target-dependent tumor growth inhibition by **MRTX1719** in an *MTAP*-del xenograft efficacy model of lung cancer.

Chemistry. A versatile synthesis was developed via the preparation of late stage phthalazinone intermediates **32** and **33**, from which compounds **2–31** could be prepared (Scheme 1).[45] Commercially available lactone **34** was treated with DMF-DMA in the presence of a catalytic base to produce intermediate **35**.[46] Ring expansion[47] with hydrazine hydrate afforded phthalazinone benzylamine **36**, which was further transformed[48] into benzyl chloride **37** upon treatment with isobutyl chloroformate. The first of two key intermediates, **32**, was obtained via reaction of **37** with phthalimide. The second key intermediate, **33**, was produced using standard chemical transformations to exchange the protecting group and install

Scheme 1. Synthesis of Compounds 2–31[a]

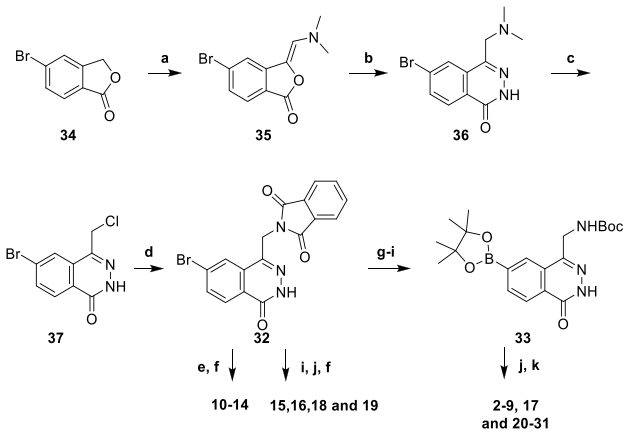

[a]Reagents and conditions: (a) DMF-DMA (6.44 equiv), ^{t}BuOK (0.10 equiv), 110 °C, 20 h. (b) Hydrazine hydrate (2.05 equiv), EtOH, 70 °C, 12 h. (c) Isobutyl chloroformate (1.20 equiv), THF, 25 °C, 6 h. (d) Potassium phthalimide (1.10 equiv), DMF, 25 °C, 1 h. (e) R_1-Bpin (1.5 equiv), Pd(dppf)Cl_2 (0.10 equiv), or Pd(dtbpf)Cl_2 (0.10 equiv), Na_2CO_3 (2.0 equiv), dioxane/H_2O, 80 °C, 2 h. (f) Hydrazine hydrate (1.00 equiv), EtOH, 80 °C, 1 h. (g) Hydrazine hydrate (1.00 equiv), EtOH, 80 °C, 16 h. (h) $(Boc)_2O$ (2.00 equiv), TEA (3.00 equiv), DCM, 25 °C, 16 h. (i) Bis(pinacolato)diboron (1.5 equiv), Pd(dppf)Cl_2 (0.10 equiv), KOAc (3.00 equiv), dioxane, 100 °C, 2 h. (j) (1) R_1-Hal (1.0 equiv), Suzuki Pd catalysts (0.1 equiv), Na_2CO_3 (2.0 equiv), dioxane/water, 80 °C, 2 h; (2) SFC separation of atropisomers if required. (k) TFA/DCM, 20 °C or HCl/MeOH, 0 °C, 0.5 h.

the boronate. With **32** and **33** in hand, compounds **2–31** were synthesized via Suzuki couplings followed by the deprotection steps depicted in Scheme 1.

The synthesis of ***MRTX1719****.* An illustrative example of a R_1-halide synthesis and coupling with the phthalazinone boronic ester **33** is shown in Scheme 2, describing the synthesis of **MRTX1719**. An S_NAr reaction with benzonitrile

Scheme 2. Synthesis of MRTX1719[a]

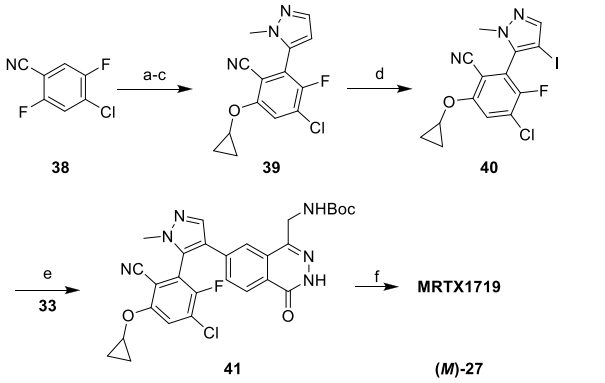

[a]Reagents and conditions: (a) Cyclopropanol (1.0 equiv), NaH, (1.05 equiv), THF, 60 °C, 1 h. (b) LDA (1.3 equiv), I_2 (2.0 equiv), THF, −78 to 25 °C, 12 h. (c) 1-Methyl-5-(4,4,5,5-tetramethyl-1,3,2-dioxaborolan-2-yl)-1*H*-pyrazole (1.4 equiv), Pd(dtbpf)Cl_2 (0.1 equiv), Na_2CO_3 (2 equiv), dioxane/water, 80 °C, 12 h. (d) NIS (2 equiv), AcOH, 80 °C, 1 h. (e) **33** (1.3 equiv), cataCXium-A-Pd-G3 (0.1 equiv), CsF (6 equiv), dioxane/water, 60 °C, 12 h. (f) (a) chiral separation of atropisomers by SFC; (b) TFA/DCM, 25 °C, 0.5 h.

https://doi.org/10.1021/acs.jmedchem.1c01900
J. Med. Chem. XXXX, XXX, XXX−XXX

38 and cyclopropanol, followed by iodination and Suzuki coupling with 1-methyl-5-(4,4,5,5-tetramethyl-1,3,2-dioxaborolan-2-yl)-1*H*-pyrazol, gave intermediate **39**. Regioselective iodination of **39** at the pyrazole C-4 position provided **40** in 62% yield. A subsequent Suzuki coupling of boronate **33** with **40** in the presence of cataCXium-A-Pd-G3 precatalyst gave fully assembled molecule **41** as a mixture of atropisomers. The atropisomers were separated using chiral prep-SFC, and acid-mediated Boc cleavage returned **MRTX1719**.

CONCLUSIONS

The identification of the PRMT5•MTA complex as a potentially tumor-selective target for therapeutic intervention provided the challenge to identify compounds that specifically bound the complex. In the approach described here, a successful FBLD program led to the discovery of a potent, selective inhibitor of the PRMT5•MTA complex, **MRTX1719**, currently in IND-enabling studies.

An SPR screen of three fragment libraries identified 24 hits with PRMT5•MTA saturable K_Ds, with several suggesting selectivity over PRMT5•SAM. One of the hits, a phthalazinone fragment (**F1**) having a PRMT5•MTA K_D = 10 μM and PRMT5•SAM K_D = 50 μM, was cocrystallized with PRMT5-MEP50 in the presence of MTA, confirming binding to the PRMT5•MTA complex. Through a process of SBDD-supported fragment growing, a series of analogues functionalized on the 6-position of the phthalazinone scaffold identified compound **9**, making a productive H-bond interaction with the Leu312 backbone, increasing potency to 300 nM in a PRMT5 methyltransferase biochemical assay in the presence of 2 μM MTA. In the absence of MTA, the IC_{50} = 5.76 μM. Further design improved biochemical and cellular potency and identified **MRTX1719**, which binds to the PRMT5•MTA complex with K_D = 0.140 pM and a long dissociation half-life of 14 days, with 67-fold selectivity over PRMT5•SAM. In matched-pair cellular assays, **MRTX1719** demonstrated HCT116 *MTAP*-del SDMA IC_{50} of 8 nM and HCT116 *MTAP*-del viability IC_{50} of 12 nM, with 82-fold and 74-fold selectivity over the corresponding HCT116 *MTAP*-WT isogenic pairs. **MRTX1719** demonstrated moderate to high oral bioavailability (41−80%) across preclinical species, and in a mouse Lu-99 tumor xenograft model of lung cancer, **MRTX1719** orally administered daily until day 21 inhibited tumor growth 60−88% in a concentration-dependent manner. Inhibition of the PRMT5-dependent SDMA protein modification biomarker (86−98%) was also observed in the tumors taken at the end of the study. Accordingly, **MRTX1719** was nominated as a development candidate and is currently in IND enabling studies. Selective inhibition of the PRMT5•MTA complex by **MRTX1719** in cancers with homozygous deletion of the *MTAP* gene may represent a precision medicine for the treatment of *MTAP*-del cancers, including a high percentage of non-small cell lung cancer, mesothelioma, pancreatic ductal adenocarcinoma, head and neck squamous cell carcinoma, urothelial carcinoma, and other cancers.[49]

EXPERIMENTAL SECTION

General Procedures. All final compounds were purified to ≥95% purity by either high-performance liquid chromatography (HPLC) or supercritical fluid chromatography (SFC). Purity was determined by HPLC and additional structural characterization was performed by proton NMR, carbon NMR, and high-resolution mass spectrometry as described below. All chemicals were purchased from commercial suppliers and used as received unless otherwise indicated. Proton nuclear magnetic resonance (^{1}H NMR) spectra were recorded on Bruker Avance 400 MHz spectrometers. Chemical shifts are expressed in δ ppm and are calibrated to the residual solvent peak: proton (e.g., $CDCl_3$, 7.27 ppm). Coupling constants (J), when given, are reported in hertz. Multiplicities are reported using the following abbreviations: s = singlet, d = doublet, dd = doublet of doublets, t = triplet, q = quartet, m = multiplet (range of multiplet is given), br = broad signal, dt = doublet of triplets. Carbon nuclear magnetic resonance (^{13}C NMR) spectra were recorded using a Bruker Avance HD spectrometer at 100 MHz. Chemical shifts are reported in parts per million (ppm) and are calibrated to the solvent peak: carbon ($CDCl_3$, 77.23 ppm). The purity for test compounds was determined by high-performance liquid chromatography (HPLC) on a LC-20AB Shimadzu instrument. HPLC conditions were as follows: Kinetex C18 LC column 4.6 mm × 50 mm, 5 μm, 10%−80% ACN (0.0375% TFA) in water (0.01875% TFA), 4 min run, flow rate 1.5 mL/min, UV detection (λ = 220, 215, 254 nm), or XBridge C18, 2.1 mm × 50 mm, 5 μm, 10%−80% ACN in water buffered with 0.025% ammonia, 4 min run, flow rate 0.8 mL/min, UV detection (λ = 220, 215, 254 nm). The mass spectra were obtained using liquid chromatography mass spectrometry (LC-MS) on a LCMS-2020 Shimadzu instrument using electrospray ionization (ESI). LCMS conditions were as follows: Kinetex EVO C18 30 mm × 2.1 mm, 5 μm, 5%−95% ACN (0.0375% TFA) in water (0.01875% TFA), 1.5 min run, flow rate 1.5 mL/min, UV detection (λ = 220, 254 nm), or Kinetex EVO C18 2.1 mm × 30 mm, 5 μm, 5%−95% ACN in water buffered with 0.025% ammonia, 1.5 min run, flow rate 1.5 mL/min, and UV detection (λ = 220, 254 nm). High resolution mass measurements were carried out on an Agilent 1290LC and 6530Q-TOF series with ESI. Optical rotation data were recorded on an Anton Paar MCP500 [length = 1 dm, sodium lamp, λ (nm) = 589, temperature = 25 °C]. The SFC purity was determined with a Shimadzu LC-30ADsf. Melting point data were recorded on a Mettler Toledo MP70 [start temperature = 65 °C, end temperature = 255 °C, rate = 3.0 °C/min].

*(Z)-5-Bromo-3-((dimethylamino)methylene)isobenzofuran-1(3H)-one (**35**).* A mixture of 5-bromoisobenzofuran-1(3*H*)-one (**34**) (50.0 g, 235 mmol, 1.00 equiv), DMF-DMA (180 g, 1.51 mol, 201 mL, 6.44 equiv), and ^{t}BuOK (2.63 g, 23.5 mmol, 0.10 equiv) was degassed and purged with N_2 3 times and then stirred at 110 °C for 20 h under a N_2 atmosphere. After such time, the reaction mixture was concentrated under reduced pressure to remove the DMF-DMA, and the formed residue was stirred in petroleum ether (100 mL) at 25 °C for 30 min. The formed solid was filtered and the filter cake stirred in ethyl acetate (200 mL) at 80 °C for 12 h, filtered, and the filter cake was dried under reduced pressure to give **35** (39.0 g, 120 mmol, 51% yield, 82% purity) as a red solid. LCMS $[M + 1]^+$ = 270.1. ^{1}H NMR (400 MHz, DMSO-d_6) δ 7.97 (d, J = 1.2 Hz, 1H), 7.61−7.59 (d, J = 8.0, 1H), 7.30−7.27 (dd, J = 8.0 and 1.2 Hz, 1H), 3.10 (s, 6H).

*6-Bromo-4-((dimethylamino)methyl)phthalazin-1(2H)-one (**36**).* To a mixture of **35** (39.0 g, 119 mmol, 82% purity, 1.00 equiv) in EtOH (650 mL) was added hydrazine hydrate (12.5 g, 245 mmol, 12.1 mL, 2.05 equiv) at 25 °C. The mixture was degassed with N_2 then stirred at 25 °C for 0.5 h and then at 70 °C for 12 h. After such time, the reaction mixture was filtered and the solid was dried to give **36** (30.0 g, 105 mmol, 88% yield) as a yellow solid. LCMS $[M + 1]^+$ = 282.1. ^{1}H NMR (400 MHz, DMSO-d_6) δ 12.6 (s, 1H), 8.33 (s, 1H), 8.14−8.12 (d, J = 8.4 Hz, 1H), 8.00−7.98 (m, 1H), 3.61 (s, 1H), 2.18 (s, 1H).

*6-Bromo-4-(chloromethyl)phthalazin-1(2H)-one (**37**).* A mixture of **36** (15.0 g, 53.2 mmol, 1.00 equiv) in THF (187 mL) and degassed with N_2 3 times before being cooled to 0 °C. Isobutyl carbonochloridate (8.71 g, 63.80 mmol, 8.38 mL, 1.20 equiv) was then added dropwise and the mixture stirred at 25 °C for 6 h under N_2. After such time, the mixture was cooled to 0 °C before HCl (0.5 M, 250 mL) was added maintaining a temperature between 0 and 10 °C. After the addition was complete the solid was filtered, washed with THF (30 mL × 3), and dried to afford a **37** (11.0 g, 37.56 mmol, 71% yield) as a yellow solid. LCMS $[M + 1]^+$ = 256.1. ^{1}H NMR (400 MHz, DMSO-d_6) δ 12.9 (s, 1H), 8.29 (d, J = 1.6 Hz, 1H), 8.19−8.17

https://doi.org/10.1021/acs.jmedchem.1c01900
J. Med. Chem. XXXX, XXX, XXX−XXX

(d, J = 8.0 Hz, 1H),8.06−80.4 (dd, J = 8.0 Hz and 1.6 Hz, 1H), 5.06 (s, 2H).

*2-((7-Bromo-4-oxo-3,4-dihydrophthalazin-1-yl)methyl)-isoindoline-1,3-dione (**32**).* To a mixture of **37** (8.06 g, 27.5 mmol, 1.00 equiv) in DMF (160 mL) was added potassium phthalimide (5.61 g, 30.3 mmol, 1.10 equiv) and stirred at 25 °C for 1 h. After such time, the mixture was washed with HCl (0.5 M, 100 mL), filtered, and the solid washed with satd $NaHCO_3$. (30 mL × 2), pure water (30 mL × 2) and then triturated with EtOH (15 mL) at 70 °C for 1 h. The solid was then filtered and dried to give **32** (8.30 g, 17.9 mmol, 65% yield, 83% purity) as a yellow solid. LCMS $[M + 1]^+$ = 384.1/386.1. ^{1}H NMR (400 MHz, DMSO-d_6) δ 12.6 (s, 1H), 8.43 (s, 1H), 8.18−8.16 (d, J = 8.0 Hz, 1H), 8.08 (d, J = 8.0 Hz, 1H), 7.95−7.89 (m, 4H), 5.18 (s, 2H).

*tert-Butyl ((4-Oxo-7-(4,4,5,5-tetramethyl-1,3,2-dioxaborolan-2-yl)-3,4-dihydrophthalazin-1-yl)methyl)carbamate (**33**).* A solution of **32** (3.00 g, 7.81 mmol, 1.00 equiv) and hydrazine hydrate (1.60 g, 31.2 mmol, 1.55 mL, 4.00 equiv) was stirred at 80 °C for 2 h. After such time, the mixture was allowed to cool and then was concentrated under reduced pressure. The concentrated residue was washed with water and triturated with ethyl alcohol at 25 °C to give 4-(aminomethyl)-6-bromo-2*H*-phthalazin-1-one (1.95 g, 7.67 mmol, 98% yield) as a white solid. LCMS $[M + 1]^+$ = 256.1. To a solution of 4-(aminomethyl)-6-bromo-2*H*-phthalazin-1-one (1.90 g, 7.48 mmol, 1.00 equiv) and triethylamine (2.27 g, 22.4 mmol, 3.12 mL, 3.00 equiv) in dichloromethane (40 mL) was added di-*tert*-butyl dicarbonate (3.26 g, 15.0 mmol, 3.44 mL, 2.00 equiv). The mixture was stirred at 25 °C for 2 h, filtered, and concentrated under reduced pressure. The concentrated residue was triturated with dichloromethane (40 mL) and then filtered and dried to give *tert*-butyl-*N*-[(7-bromo-4-oxo-3*H*-phthalazin-1-yl)methyl]carbamate (1.97 g, 5.56 mmol, 74% yield) as a white solid and taken on to the next step without further purification. LCMS $[M + 1]^+$ = 356.1. ^{1}H NMR (400 MHz, DMSO-d_6) δ 12.71 (s, 1H), 8.26 (br s, 1H), 8.16 (br d, J = 8.0 Hz, 1H), 8.02 (br d, J = 8.0 Hz, 1H), 7.46 (br s, 1H), 4.41 (br d, J = 4.4 Hz, 2H), 1.40 (br s, 9H). A mixture of *tert*-butyl-*N*-[(7-bromo-4-oxo-3*H*-phthalazin-1-yl)methyl]carbamate (1.30 g, 2.75 mmol, 1.00 equiv), bis(pinacolato)diboron (1.049 g, 4.13 mmol, 1.50 equiv), Pd(dtbpf)Cl_2 (0.201 g, 0.275 mmol, 0.10 equiv), and KOAc (0.810 g, 8.25 mmol, 3.00 equiv) in dioxane (260 mL) was degassed and purged with N_2. The mixture was then stirred at 100 °C for 2 h. After such time, the mixture was filtered, concentrated, and the residue triturated with petroleum ether/ethyl acetate 10/1 (4 mL) at 25 °C for 1 h. The solid was then filtered and dried to give **33** (680 mg, 1.62 mmol, 59% yield) as a brown solid. LCMS $[M + 1]^+$ = 402.3. ^{1}H NMR (400 MHz, $CDCl_3$) δ 12.62 (s, 1H), 8.25 (s, 2H), 8.01−8.13 (m, 1H), 7.21−7.45 (m, 1H), 4.34−4.63 (m, 2H), 1.42 (s, 9H), 1.32 (s, 12H).

*4-(Aminomethyl)-6-(1-methylpyrazol-4-yl)-2H-phthalazin-1-one hydrochloride (**9**).* A mixture of 4-bromo-1-methyl-pyrazole (200 mg, 1.24 mmol, 1.00 equiv), **33** (548 mg, 1.37 mmol, 1.10 equiv), sodium carbonate (263 mg, 2.48 mmol, 2.00 equiv), and Pd(dppf)Cl_2 (81 mg, 0.124 mmol, 0.10 equiv) in dioxane (3.0 mL) and water (0.6 mL) was degassed and stirred at 80 °C for 2 h under a nitrogen atmosphere. After such time, the reaction mixture was diluted with ethyl acetate (50 mL) and filtered. The filtrate was concentrated under reduced pressure, and the residue was purified by column chromatography (SiO_2, ethyl acetate/petroleum ether 2−25%) to give *tert*-butyl *N*-[[7-(1-methylpyrazol-4-yl)-4-oxo-3*H*-phthalazin-1-yl]methyl]carbamate (35 mg, 0.10 mmol) as a white solid. LCMS $[M + 1]^+$ = 356.2. To a solution of *tert*-butyl *N*-[[7-(1-methylpyrazol-4-yl)-4-oxo-3*H*-phthalazin-1-yl]methyl]carbamate (35 mg, 0.10 mmol, 1.00 equiv) in dichloromethane (1.0 mL) was added trifluoroacetic acid (0.37 mL, 4.92 mmol, 50.0 equiv). The mixture was stirred at 20 °C for 1 h. The reaction mixture was concentrated under reduced pressure. The residue was diluted with DMF (3.5 mL) and purified by prep-HPLC (HCl condition) to give **9** (5 mg, 19 μmol, 20% yield) as a white solid, 97% purity, retention time 4.05 min, B in A 0−60% (10 min method). ^{1}H NMR (400 MHz, DMSO-d_6) δ 12.82 (s, 1H), 8.64 (br s, 3H), 8.52 (s, 1H), 8.23 (d, J = 8.4 Hz, 1H), 8.21 (s, 1H), 8.14−8.08 (m, 2H), 4.48 (br d, J = 5.6 Hz, 2H), 3.91 (s, 3H). ^{13}C NMR (101 MHz, DMSO-d_6) δ 159.4, 146.8, 137.6, 137.1, 129.6, 129.4, 128.1, 126.6, 125.3, 120.8, 120.1, 42.8, 38.8. HRMS (ESI, +ve ion) m/z calcd for $C_{13}H_{14}N_5O^+$ $[M + H^+]$ 256.1193, found 256.1174.

*Synthesis of **MRTX1719** ((**M**)-**27**). 4-Chloro-6-(cyclopropoxy)-3-fluoro-2-(2-methylpyrazol-3-yl)benzonitrile (**39**).* To a solution of cyclopropanol (14.3 g, 247 mmol, 1.00 equiv) in THF (400 mL) was added sodium hydride in mineral oil (10.4 g, 259 mmol, 60% purity, 1.05 equiv) at 0 °C. After stirring for 30 min, 4-chloro-2,5-difluorobenzonitrile (**38**) (42.8 g, 247 mmol, 1.00 equiv) was added to the reaction mixture. The mixture was stirred at 60 °C for 1 h. The cooled reaction mixture was then diluted with water (200 mL) and extracted with ethyl acetate (200 mL × 3). The combined organic phase was washed with brine (200 mL), dried over anhydrous sodium sulfate, filtered, and concentrated to give a residue. The residue was purified by column chromatography (SiO_2, ethyl acetate/petroleum ether 0−5%) to give 4-chloro-2-(cyclopropoxy)-5-fluoro-benzonitrile (31.5 g, 149 mmol, 60% yield) as a white solid. ^{1}H NMR (400 MHz, $CDCl_3$) δ 7.38 (d, J = 6.0 Hz, 1H), 7.34 (d, J = 8.0 Hz, 1H), 3.86−3.79 (m, 1H), 0.93−0.88 (m, 4H). To a solution of 4-chloro-2-(cyclopropoxy)-5-fluoro-benzonitrile (6.40 g, 30.2 mmol, 1.00 equiv) in THF (200 mL) was added lithium diisopropylamide (2.00 M in THF, 22.7 mL, 1.50 equiv) at −78 °C. After stirring for 0.5 h, iodine (15.4 g, 60.5 mmol, 2.00 equiv) in THF (200 mL) was added to the reaction mixture in a dropwise fashion. The reaction mixture was then stirred at 25 °C for 12 h. After such time, the reaction mixture was quenched with water (200 mL) and extracted with ethyl acetate (200 mL × 3). The combined organic phases were washed with brine (200 mL), dried over anhydrous sodium sulfate, filtered, and concentrated to give a residue. The residue was purified by column chromatography (SiO_2, ethyl acetate/petroleum ether 0−5%) to give 4-chloro-6-cyclopropoxy-3-fluoro-2-iodobenzonitrile (9.10 g, 27.0 mmol, 89% yield) as a brown solid. ^{1}H NMR (400 MHz, $CDCl_3$) δ 7.39 (d, J = 6.0 Hz, 1H), 3.87−3.81 (m, 1H), 0.91 (d, J = 4.4 Hz, 4H). A mixture of 4-chloro-6-(cyclopropoxy)-3-fluoro-2-iodo-benzonitrile (14.0 g, 41.5 mmol, 1.00 equiv), 1-methyl-5-(4,4,5,5-tetramethyl-1,3,2-dioxaborolan-2-yl)pyrazole (14.7 g, 70.5 mmol, 1.70 equiv), Pd(dtbpf)Cl_2 (2.70 g, 4.15 mmol, 0.10 equiv), and sodium carbonate (8.79 g, 83.0 mmol, 2.00 equiv) in dioxane (140 mL) and water (28 mL) was degassed with nitrogen and stirred at 80 °C for 12 h under a nitrogen atmosphere. After such time, the cooled reaction mixture was concentrated under reduced pressure. The formed residue was diluted with water (50 mL) and extracted with ethyl acetate (100 mL × 3). The combined organic extracts were then washed with brine (50 mL), dried over anhydrous sodium sulfate, filtered, and concentrated. The residue was purified by column chromatography (SiO_2, ethyl acetate/petroleum ether 2−20%) to give **39** (8.50 g, 27.7 mmol, 67% yield) as a yellow solid. ^{1}H NMR (400 MHz, $CDCl_3$) δ 7.60 (d, J = 2.0 Hz, 1H), 7.48 (d, J = 6.0 Hz, 1H), 6.49 (d, J = 2.0 Hz, 1H), 4.09 (s, 1H), 3.81 (d, J = 1.2 Hz, 3H), 0.93 (d, J = 4.4 Hz, 4H).

*4-Chloro-6-(cyclopropoxy)-3-fluoro-2-(4-iodo-2-methyl-pyrazol-3-yl)benzonitrile (**40**).* A mixture of **39** (5.60 g, 19.2 mmol, 1.00 equiv) and *N*-iodosuccinimide (8.64 g, 38.4 mmol, 2.00 equiv) in acetic acid (60 mL) was degassed with nitrogen and stirred at 80 °C for 3 h under a nitrogen atmosphere. After such time, the cooled reaction mixture was concentrated under reduced pressure to give a residue. The residue was then diluted with water (20 mL) and extracted with ethyl acetate (50 mL × 3). The combined organic phases were washed with saturated aqueous sodium bicarbonate (50 mL × 2) then brine (50 mL), dried over anhydrous sodium sulfate, filtered, and concentrated. The formed residue was purified by column chromatography (SiO_2, ethyl acetate/petroleum ether 5−25%) to give **40** (5.00 g, 12.0 mmol, 62% yield) as a yellow solid. ^{1}H NMR (400 MHz, $CDCl_3$) δ 7.65 (s, 1H), 7.56 (d, J = 6.0 Hz, 1H), 3.93−3.87 (m, 1H), 3.83 (s, 3H), 0.98−0.93 (m, 4H).

*(±)-tert-Butyl N-[[7-[5-[5-Chloro-2-cyano-3-(cyclopropoxy)-6-fluoro-phenyl]-1-methyl-pyrazol-4-yl]-4-oxo-3H-phthalazin-1-yl]-methyl]carbamate (**41**).* A mixture of **33** (1.38 g, 3.45 mmol, 1.20 equiv), **40** (1.20 g, 2.87 mmol, 1.00 equiv), cataCXium-A-Pd-G3 precatalyst (209 mg, 0.29 mmol, 0.10 equiv), and CsF (2.62 g, 17.2

https://doi.org/10.1021/acs.jmedchem.1c01900
J. Med. Chem. XXXX, XXX, XXX−XXX

mmol, 6.00 equiv) in 1,4-dioxane (16 mL) and water (4 mL) was purged with nitrogen 3 times then stirred at 60 °C for 12 h under a nitrogen atmosphere. After such time, the reaction mixture was concentrated under reduced pressure and the formed residue was diluted with water (20 mL) and extracted with ethyl acetate (20 mL × 3). The combined organic extracts were washed with brine (20 mL), dried over anhydrous sodium sulfate, filtered, and concentrated to give a residue. The residue was purified by column chromatography (SiO_2, ethyl acetate/petroleum ether 10−33%) to give **41** (3.00 g, 5.15 mmol, 60% yield) as an off-white solid.

MRTX1719 *(M)-2-[4-[4-(Aminomethyl)-1-oxo-2H-phthalazin-6-yl]-2-methyl-pyrazol-3-yl]-4-chloro-6-(cyclopropoxy)-3-fluoro-benzonitrile Hydrochloride* ***((M)-27B)****.* The atropisomer mixture of **41** (3.00 g) was separated by chiral prep SFC (column: Daicel Chiralpak IC (250 mm × 30 mm,10 μm); mobile phase [0.1% NH_4OH in IPA, %B: 35%] to afford (*P*)-*tert*-butyl *N*-[[7-[5-[5-chloro-2-cyano-3-(cyclopropoxy)-6-fluoro-phenyl]-1-methyl-pyrazol-4-yl]-4-oxo-3*H*-phthalazin-1-yl]methyl]carbamate, the first eluting peak (1.00 g, 1.77 mmol, 33% yield) as a white solid and (*M*)-*tert*-butyl *N*-[[7-[5-[5-chloro-2-cyano-3-(cyclopropoxy)-6-fluoro-phenyl]-1-methyl-pyrazol-4-yl]-4-oxo-3*H*-phthalazin-1-yl]methyl]carbamate, the second eluting peak (1.23 g, 2.18 mmol, 41% yield) as a white solid. LC-MS $[M + 1]^+$ = 565.3. To a solution of (*M*)-*tert*-butyl *N*-[[7-[5-[5-chloro-2-cyano-3-(cyclopropoxy)-6-fluoro-phenyl]-1-methyl-pyrazol-4-yl]-4-oxo-3*H*-phthalazin-1-yl]methyl]carbamate (1.23 g, 2.18 mmol, 1.00 equiv) in dichloromethane (9 mL) was added trifluoroacetic acid (3.69 mL, 49.8 mmol, 22.9 equiv), and the resulting slurry was stirred at 25 °C for 0.5 h. The reaction mixture was concentrated under reduced pressure, and the formed residue was purified by prep-HPLC (HCl condition) to give **MRTX1719** (1.05 g, 1.88 mmol, 86% yield) as a yellow solid, 97.5% HPLC purity, Retention time 3.66 min, B in A 10−80% (10 min method); >99% ee by SFC, Shimadzu LC-30ADsf, column: IC-3, mobile phase EtOH (0.05% DEA) 40% isocratic, 5 min, 35 °C, 2.8 min RT; mp 237.0 °C; $[\alpha]D$ (20 °C) = −34.97 deg cm^3 g^{-1} dm^{-1} (c = 0.002 g cm^{-3}, MeOH). ^1H NMR (400 MHz, DMSO-d_6) δ 12.88 (s, 1H), 8.60 (br s, 3H), 8.39 (s, 1H), 8.14 (d, J = 8.4 Hz, 1H), 8.02 (d, J = 6.0 Hz, 1H), 7.86 (d, J = 1.6 Hz, 1H), 7.47 (dd, J = 1.6, 8.4 Hz, 1H), 4.42−4.30 (m, 2H), 4.24 (tt, J = 2.8, 6.0 Hz, 1H), 3.78 (s, 3H), 0.96−0.87 (m, 2H), 0.87−0.76 (m, 2H). ^{19}F NMR (400 MHz, DMSO-d_6) δ −122.3 (s, 1F). ^{13}C NMR (101 MHz, CD_3OD) δ 160.4, 158.3, 151.4, 149.0, 139.1, 138.2, 130.1, 130.0, 128.7, 128.6, 128.5, 127.1, 125.7, 122.2, 121.3, 118.0, 112.3, 101.9, 53.2, 38.6, 36.3, 5.4. HRMS (ESI, +ve ion) m/z calcd for $C_{23}H_{19}ClFN_6O_2^+$ $[M + H^+]$ 465.1237, found 465.1233.

Biochemical Methyl Transferase Assay. The assay uses purified human PRMT5 enzyme to convert *S*-adenosyl-L-[methyl-^3H]-methionine plus histone H4 L-arginine to *S*-adenosyl-L-homocysteine plus histone H4 [methyl-^3H]-L-arginine. The assay was carried out using streptavidin-coated FlashPlates (PerkinElmer), which contain a scintillant embedded in the plastic of the plate. The histone H4 peptide substrate was conjugated with biotin, which binds to the streptavidin-coated well of the plate, placing the H4 peptide in close proximity to the side of the well and the scintillant. The transfer of the tritiated methyl group from *S*-adenosyl-L-[methyl-^3H]methionine to the bound histone H4 peptide generated a radiolabeled histone H4, which was quantified by measuring radioactivity in a scintillation counter to determine the activity of PRMT5 enzyme in the presence and absence of compound. The assay reactions were also conducted in the presence and absence of MTA to determine whether the compounds exhibit MTA-cooperative activity. Briefly, compounds were solubilized in 100% DMSO at a top concentration of 10 mM. For IC_{50} determinations, the initial starting concentration for the serial dilutions of each compound was 50 μM. Control samples lacking compound, PRMT5/MEP50 complex, or various reaction components were also prepared and processed in parallel with compound test samples. SAH was used as a positive control for assay validation. To measure PRMT5 inhibitory activity, 3 nM PRMT5/MEP50 complex (Reaction Biology Corporation) was preincubated with test compound in assay buffer containing 40 nM histone H4 peptide (amino acids 1−15)−biotin conjugate for 20 min at room temperature. The enzymatic reaction was initiated by adding 1 μM tritiated SAM (final concentration), and the reaction was allowed to proceed for 20 min. The reaction was stopped, and the amount of bound, tritiated H4 peptide in each sample was determined using a scintillation counter. The IC_{50} value for each compound was calculated from each 10-point dose−response curve for samples plus and minus MTA using GraphPad Prism software.

HCT116 Homozygous *MTAP* Knockout Cell Line: HCT116 *MTAP*-del. HCT116 cells were genetically engineered to knock out the function of both *MTAP* alleles using a CRISPR/Cas9 system and an sgRNA targeting the *MTAP* gene. Following Cas9/MTAP sgRNA transduction, clones were screened to confirm that each allele of the *MTAP* gene had been inactivated (i.e., homozygous *MTAP* knockout), creating an *MTAP*-deficient cell. Clone 2−15, confirmed to have a homozygous *MTAP* knockout, was used in cell-based assays to assess the inhibition of PRMT5-dependent SDMA and antiproliferative activity.

HCT116 *MTAP*-WT and *MTAP*-del Viability Assay. Viability assays were performed using HCT116 *MTAP*-WT and HCT116 *MTAP*-del cell lines. Control samples were analyzed in parallel. On day 0, 250 HCT116 *MTAP*-WT or HCT116 *MTAP*-del cells were seeded in 96-well plates in McCoy's 5A supplemented with 10% fetal bovine serum and pen/strep, and the cells were incubated overnight at 37 °C plus 5% CO_2. The following day, cells were treated with DMSO vehicle control or a dose−response of test compound and incubated at 37 °C plus 5% CO_2 for 5 days. On day 6, the cells were trypsinized and split 1:20 into new 96-well plates with fresh medium containing the same concentration of test compound and incubated for an additional 5 days at 37 °C plus 5% CO_2. On day 11, the viability of the cells was measured using a CTG assay kit (CellTiter-Glo; Promega catalogue no. G7573) in accordance with the manufacturer's instructions. The IC_{50} values for each compound after 10 days of treatment were calculated using GraphPad PRISM software.

HCT116 *MTAP*-WT and *MTAP*-del SYM11 In-Cell Western Assay. In-Cell Western assays were performed using HCT116 *MTAP*-WT and HCT116 *MTAP*-del cell lines by measuring the PRMT5-dependent symmetric dimethyl arginine (SDMA) signal. Control samples were analyzed in parallel. On day 0, 2000 HCT116 *MTAP*-WT and HCT116 *MTAP*-del cells were seeded in 96-well plates in McCoy's 5A supplemented with 10% fetal bovine serum and pen/strep, and the cells were incubated overnight at 37 °C plus 5% CO_2. The following day, cells were treated with DMSO vehicle control or a dose−response of test compounds and incubated at 37 °C plus 5% CO_2 for 4 days. After 4 days of treatment, the cells were fixed by adding 50 μL of a 4% paraformaldehyde solution to each well, and the cells were incubated for 20 min at room temperature. The paraformaldehyde solution was then removed, and 150 μL of ice-cold methanol was added and the plate stored at −20 °C for 10 min. After such time, the methanol was removed and 150 μL of Odyssey Blocking Buffer + 0.05% Tween-20 was added, and the plate was incubated at room temperature with shaking for 1 h. To each test well, 50 μL of SYM11 antibody (Millipore 07-413) diluted 1:500 in Odyssey Blocking Buffer + 0.05% Tween-20 was added, and the plate was placed at 4 °C overnight. The primary SYM11 antibody solution was removed by aspiration, and the wells were washed 3 times with phosphate buffered saline containing 0.1% Tween-20 (PBST). A 50 μL aliquot of a goat anti-rabbit IRDye 800CW secondary antibody (Li-Cor 926-32211) diluted 1:800 and nuclear stain DRAQ5 (Biostatus Limited) diluted 1:10000 in Odyssey Blocking Buffer + DRAQ5 + 0.05% Tween-20 was added, and the plate was stored for 2 h in the dark at room temperature. The secondary antibody solution was removed by aspiration, and the wells were washed 3 times with PBST. The SYM11 signal and the DRAQ5 signal were quantified using a Li-Cor Odyssey machine reading at 800 nM and 700 nM, respectively. The SYM11/DRAQ5 ratio was used to calculate the inhibition of SDMA as percent of DMSO control.

Xenograft Study. (2-Hydroxypropyl)-β-cyclodextrin (H5784), (hydroxypropyl)methyl cellulose 4000 cps (M0512), and Tween 80 (P8074) were purchased from Sigma-Aldrich (St. Louis, MO).

https://doi.org/10.1021/acs.jmedchem.1c01900
J. Med. Chem. XXXX, XXX, XXX−XXX

Roswell Park Memorial Institute 1640 (RPMI) medium (11875-093), HEPES ((4-(2-hydroxyethyl)-1-piperazineethanesulfonic acid), 15630-080), Dulbecco's phosphate-buffered saline (DPBS, 14190-136), and sodium pyruvate (11360-070) were obtained from Gibco/Thermo Fisher Scientific (Waltham, MA). Fetal bovine serum (FBS) was obtained from Corning (35-011-CV, Corning, NY). Antibiotic−antimycotic solution was obtained from Caisson Laboratories (ABL02, Smithfield, UT). Pierce radioimmunoprecipitation assay (RIPA) lysis buffer (89901), 10× HALT (PI78443), and phenylmethanesulfonyl fluoride (PMSF) (ICN19538105) were purchased from ThermoFisher (Waltham, MA). Sodium orthovanadate (S6508-10G) was purchased from Sigma-Aldrich (St. Louis, MO). The following antibodies were used at the indicated dilution: SDMA (1:1000; 13222S; Cell Signaling Technology, Danvers, MA), β-actin (1:2000; ab8226; Abcam, Cambridge, UK), IRDye 680RD goat anti-rabbit (1:10 000; 926-68071; LiCor, Lincoln NE), and IRDye 800CW goat antimouse (1:10 000; 926-32210; LiCor, Lincoln NE).

The Lu-99 cell line (RCB1900) was obtained from RIKEN BioResource Research Center (Tsukuba, Japan) and grown in RPMI 1640 media containing 10% fetal bovine serum, 10 mM HEPES, 1 mM sodium pyruvate, and 1% antibiotic−antimycotic.

Mouse studies were conducted in compliance with all applicable regulations and guidelines of the Institutional Animal Care and Use Committee (IACUC) from the National Institutes of Health (NIH). Mice were maintained under pathogen-free conditions and food and water were provided ad libitum. 6−8-week-old female Hsd:Athymic Nude-*Foxn1*^{nu} mice (Envigo, San Diego) were injected subcutaneously, with 5.0×10^6 Lu-99 tumor cells in 100 μL of PBS and Matrigel matrix (Corning 356237; Discovery Labware, MA) in the right hind flank of each mouse (50:50 cells:Matrigel). Mouse health was monitored daily, and caliper measurements began when tumors were palpable. Tumor volume measurements were determined utilizing the formula $0.5 \times L \times W^2$, in which L refers to length and W refers to width of each tumor. When tumors reached an average tumor volume of ∼180 mm, mice were randomized into treatment groups. **MRTX1719** was formulated in 0.5% methylcellulose (4000 cps) + 0.2% Tween 80 in water once per week and stored at room temperature protected from light. Mice were orally administered vehicle or **MRTX1719** PO at the indicated doses and schedules. Mice were monitored daily, and tumor volumes and body weights were measured 2 or 3 times per week. Percent tumor growth inhibition (% TGI) was calculated using the following formula: (1 − (Final Drug Treated Tumor Volume − Initial Drug Treated Tumor Volume)/(Final Vehicle Treated Tumor Volume − Initial Vehicle Treated Tumor Volume)) × 100.

Whole blood was collected to measure plasma concentrations of **MRTX1719** and assess pharmacokinetic properties of **MRTX1719** at specific time points postdose. Blood (∼50 μL) was collected via submandibular draw into a heparinized tube (BD Microtainer 365965; Becton Dickinson, NJ) and immediately inverted to mix. Heparinized blood was then centrifuged at 4000 rpm for 6 min to separate plasma and cellular fractions. The separated plasma was transferred to a polypropylene 96-well plate and immediately stored at −20 °C until analysis.

At the end of study, mice were humanely sacrificed, and tumors were surgically removed and immediately cut in half. One half was transferred to a Lysing Matrix A tube (6910100; MP Biomedicals, OH), and the other half was transferred to a screw-top microtube (19-628-3; Omni Inc., Kennesaw, GA). These tubes were immediately submerged in liquid nitrogen to snap freeze the tissue. Frozen tumor fragments were stored at −80 °C until analysis.

Immunoblotting. Tumor fragments were frozen in 2 mL screw-top microtubes with ceramic beads. An equal volume of Pierce RIPA lysis buffer with 10× HALT, 2 mM PMSF, and 1 mM sodium orthovanadate added (∼300−650 mL), and tumors were homogenized using the MP FastPrep-24 homogenizer (MP Biomedicals, Santa Ana, CA) with high-speed shaking 3−5 times for 20 s while keeping the tumor lysate on ice between cycles. After homogenization, tubes were spun at 15 000 rpm for 10 min at 4 °C and the supernatant was collected. Protein concentrations of each lysate sample were determined using a Pierce BCA protein assay kit (PI23227; ThermoFisher, Waltham, MA) per the manufacturer's instructions.

Approximately 30 mg of total protein was added to 4× sample loading buffer (161-0791; Bio-Rad, Hercules, CA) and 10× reducing agent (NP0009; Invitrogen, Carlsbad, CA). Samples were boiled for 5 min. Processed samples were then loaded onto 12% Bis-Tris 26-well gels (3450119; Bio-Rad, Hercules, CA) using MOPS running buffer (161-0788; Bio-Rad, Hercules, CA). Proteins were transferred from the gels to a nitrocellulose membrane using the iBlot 2 Dry Blotting System (IB23001; ThermoFisher, Waltham, MA) and run at 20 V for 1 min, 23 V for 4 min, and 25 V for 2 min.

Membranes were blocked with Licor Intercept TBS blocking buffer (927-60001; ThermoFisher, Waltham, MA) for 1 h at room temperature on a rocking platform. Primary antibodies were diluted in LiCor blocking buffer and incubated overnight at 4 °C on a rocking platform. Membranes were then washed three times for 10 min with Tris-buffered saline−Tween-20 (TBS-T) and incubated with LiCor IR Dye secondary antibodies for 1 h at room temperature. Membranes were washed three times for 10 min with TBS-T.

Images were acquired from probed nitrocellulose membranes using the LiCor Odyssey CLx Imaging system (LiCor, Lincoln, NE) set to the AutoScan channel for both the 700 and 800 wavelength channels to measure the signal intensity from the IRDye 680RD goat antirabbit and IRDye 800CW goat antimouse secondary antibodies, respectively. Images were imported into LiCor's Image Studio software version 4.0 and then exported for annotation. To quantify the pixel intensity for each selected protein band, the Add Rectangle tool in the image viewer was used to identify a consistently sized area of interest for each band of a given target protein as well as a representative background region of the immunoblot. The signal output column from the software subtracted the background pixel intensity, and this was used to determine the target pixel intensity for each protein band. The corrected signal intensity was determined for each target protein of interest and data were exported to Excel. Target protein normalization of each sample was determined by dividing the signal output of the target protein by the signal output of the loading control protein. Each target protein was also averaged within each vehicle or treatment group. The vehicle value was normalized to 1 by dividing all average values by the vehicle value and standard deviation was calculated from the normalized values. Percent inhibition of normalized SDMA in **MRTX1719**-treated tumors compared to vehicle-treated control tumors was calculated by dividing the average **MRTX1719**-treated normalized SDMA signal by the average vehicle-treated normalized SDMA signal and multiplying by 100. GraphPad Prism 7 (GraphPad, San Diego, CA) was used to graph the data.

■ ASSOCIATED CONTENT

Supporting Information

The Supporting Information is available free of charge at https://pubs.acs.org/doi/10.1021/acs.jmedchem.1c01900.

Synthetic experimental procedures; NMR spectra and HPLC trace of final compounds; design of the focused fragment library; PRMT5/MEP50 protein expression and purification; PRMT5-sinefungin X-ray structure; PRMT5•MTA X-ray structures for compounds **29**, **30**, and (***M***)-**31**; SPR experimental procedures and methyltransferase panel inhibition data for **MRTX1719** (PDF)

Molecular formula strings (CSV)

Accession Codes

Atomic coordinates for the X-ray structures of **F1** (PDB 7S0U), **9** (PDB 7S1Q), **MRTX1719** (PDB 7S1S), **29** (PDB 7SES), **30** (PDB 7SER), (***M***)-**31** (PDB 7S1R) bound to PRMT5•MTA, and the PRMT5•sinefungin structure (PDB 7S1P) are available from the RCSB Protein Data Bank (www.rcsb.org).

https://doi.org/10.1021/acs.jmedchem.1c01900
J. Med. Chem. XXXX, XXX, XXX−XXX

AUTHOR INFORMATION

Corresponding Author

Christopher R. Smith − *Mirati Therapeutics, San Diego, California 92121, United States;* orcid.org/0000-0002-6553-2791; Phone: (+1) 858-529-1865; Email: smthc@mirati.com

Authors

Ruth Aranda − *Mirati Therapeutics, San Diego, California 92121, United States*

Thomas P. Bobinski − *DSG, San Diego, California 92130, United States*

David M. Briere − *Mirati Therapeutics, San Diego, California 92121, United States*

Aaron C. Burns − *Mirati Therapeutics, San Diego, California 92121, United States*

James G. Christensen − *Mirati Therapeutics, San Diego, California 92121, United States*

Jeffery Clarine − *Mirati Therapeutics, San Diego, California 92121, United States*

Lars D. Engstrom − *Mirati Therapeutics, San Diego, California 92121, United States*

Robin J. Gunn − *Mirati Therapeutics, San Diego, California 92121, United States*

Anthony Ivetac − *Mirati Therapeutics, San Diego, California 92121, United States*

Ronald Jean-Baptiste − *ZoBio BV, 2333 CH Leiden, Netherlands*

John M. Ketcham − *Mirati Therapeutics, San Diego, California 92121, United States*

Masakazu Kobayashi − *ZoBio BV, 2333 CH Leiden, Netherlands*

Jon Kuehler − *Mirati Therapeutics, San Diego, California 92121, United States*

Svitlana Kulyk − *Mirati Therapeutics, San Diego, California 92121, United States*

J. David Lawson − *Mirati Therapeutics, San Diego, California 92121, United States*

Krystal Moya − *Mirati Therapeutics, San Diego, California 92121, United States*

Peter Olson − *Mirati Therapeutics, San Diego, California 92121, United States*

Lisa Rahbaek − *Mirati Therapeutics, San Diego, California 92121, United States*

Nicole C. Thomas − *Mirati Therapeutics, San Diego, California 92121, United States*

Xiaolun Wang − *Mirati Therapeutics, San Diego, California 92121, United States*

Laura M. Waters − *Mirati Therapeutics, San Diego, California 92121, United States*

Matthew A. Marx − *Mirati Therapeutics, San Diego, California 92121, United States*

Complete contact information is available at: https://pubs.acs.org/10.1021/acs.jmedchem.1c01900

Author Contributions

The manuscript was written through the contributions of all authors. All authors have given approval to the final version of the manuscript.

Notes

The authors declare no competing financial interest.

ACKNOWLEDGMENTS

We thank the following teams/people for their valuable contributions to this work: Natalie Nguyen for generating the CYP inhibition data. The IDSU chemistry team (WuXi AppTec in Wuhan, China): Tao Guo, Duan Liu, and Song Mo. CSU chemistry team (WuXi AppTec in Wuhan, China): Rongfeng Zhao, Shaojun Song, and Wenbing Ruan. In vitro ADME and PK team (WuXi Apptec in Shanghai, China): Yunting Xu, Binbin Tian. Gregg Siegal and Stephan Theisgen (ZoBio BV, J.H. Oortweg 19, 2333 CH Leiden, Netherlands) for the second SPR screen and the SPR studies for compounds **F1**, **9**, and **MRTX1719**. Rebecca Eells (Reaction Biology Corporation) for the first SPR screen. Stephan Krapp and Brantley Haigh (Proteros Biostructures GmbH, Bunsenstraße 7a, 82152 Planegg, Germany) for early enablement of SBDD in this project. All research described in this manuscript was funded by Mirati Therapeutics. The x-ray crystallography work presented herein is based upon research conducted at the Northeastern Collaborative Access Team beamlines, which are funded by the National Institute of General Medical Sciences from the National Institutes of Health (P30 GM124165). The Eiger 16M detector on 24-ID-E is funded by a NIH-ORIP HEI grant (S10OD021527). This research used resources of the Advanced Photon Source, a U.S. Department of Energy (DOE) Office of Science User Facility operated for the DOE Office of Science by Argonne National Laboratory under contract no. DE-AC02-06CH11357.

ABBREVIATIONS USED

PRMT5, protein arginine methyltransferase 5; MTAP, methylthioadenosine phosphorylase; MTA, methylthioadenosine; PK, pharmacokinetic; IV, intravenous; PO, per os (oral); SAR, structure−activity relationship; MDCK, Madin−Darby Canine Kidney cell; QD, quaque die (once daily); AUC, area under the curve; TGI, tumor growth inhibition; SFC, supercritical fluid chromatography

REFERENCES

(1) Bedford, M. T.; Clarke, S. G. Protein arginine methylation in mammals: who, what, and why. *Mol. Cell* **2009**, *33* (1), 1−13.

(2) Antonysamy, S.; Bonday, Z.; Campbell, R. M.; Doyle, B.; Druzina, Z.; Gheyi, T.; Han, B.; Jungheim, L. N.; Qian, Y.; Rauch, C.; Russell, M.; Sauder, J. M.; Wasserman, S. R.; Weichert, K.; Willard, F. S.; Zhang, A.; Emtage, S. Crystal structure of the human PRMT5:MEP50 complex. *Proc. Natl. Acad. Sci. U. S. A.* **2012**, *109* (44), 17960−17965.

(3) Friesen, W. J.; Paushkin, S.; Wyce, A.; Massenet, S.; Pesiridis, G. S.; Van Duyne, G.; Rappsilber, J.; Mann, M.; Dreyfuss, G. The methylosome, a 20S complex containing JBP1 and pICln, produces dimethylarginine-modified Sm proteins. *Mol. Cell. Biol.* **2001**, *21* (24), 8289−8300.

(4) Friesen, W. J.; Wyce, A.; Paushkin, S.; Abel, L.; Rappsilber, J.; Mann, M.; Dreyfuss, G. A novel WD repeat protein component of the methylosome binds Sm proteins. *J. Biol. Chem.* **2002**, *277* (10), 8243−8247.

(5) Karkhanis, V.; Hu, Y. J.; Baiocchi, R. A.; Imbalzano, A. N.; Sif, S. Versatility of PRMT5-induced methylation in growth control and development. *Trends Biochem. Sci.* **2011**, *36* (12), 633−641.

(6) Litzler, L. C.; Zahn, A.; Meli, A. P.; Hebert, S.; Patenaude, A. M.; Methot, S. P.; Sprumont, A.; Bois, T.; Kitamura, D.; Costantino, S.; King, I. L.; Kleinman, C. L.; Richard, S.; Di Noia, J. M. PRMT5 is essential for B cell development and germinal center dynamics. *Nat. Commun.* **2019**, *10*, 22.

(7) Wang, Y.; Zhu, T.; Li, Q.; Liu, C.; Han, F.; Chen, M.; Zhang, L.; Cui, X.; Qin, Y.; Bao, S.; Gao, F. Prmt5 is required for germ cell survival during spermatogenesis in mice. *Sci. Rep.* **2015**, *5*, 11031.
(8) Tanaka, Y.; Nagai, Y.; Okumura, M.; Greene, M. I.; Kambayashi, T. PRMT5 is required for T cell survival and proliferation by maintaining cytokine signaling. *Front. Immunol.* **2020**, *11*, 621.
(9) Andreu-Perez, P.; Esteve-Puig, R.; de Torre-Minguela, C.; Lopez-Fauqued, M.; Bech-Serra, J. J.; Tenbaum, S.; Garcia-Trevijano, E. R.; Canals, F.; Merlino, G.; Avila, M. A.; Recio, J. A. Protein arginine methyltransferase 5 regulates ERK1/2 signal transduction amplitude and cell fate through CRAF. *Sci. Signal* **2011**, *4* (190), ra58.
(10) Tee, W. W.; Pardo, M.; Theunissen, T. W.; Yu, L.; Choudhary, J. S.; Hajkova, P.; Surani, M. A. Prmt5 is essential for early mouse development and acts in the cytoplasm to maintain ES cell pluripotency. *Genes. Dev.* **2010**, *24* (24), 2772−2777.
(11) Kryukov, G. V.; Wilson, F. H.; Ruth, J. R.; Paulk, J.; Tsherniak, A.; Marlow, S. E.; Vazquez, F.; Weir, B. A.; Fitzgerald, M. E.; Tanaka, M.; Bielski, C. M.; Scott, J. M.; Dennis, C.; Cowley, G. S.; Boehm, J. S.; Root, D. E.; Golub, T. R.; Clish, C. B.; Bradner, J. E.; Hahn, W. C.; Garraway, L. A. MTAP deletion confers enhanced dependency on the PRMT5 arginine methyltransferase in cancer cells. *Science* **2016**, *351* (6278), 1214−1218.
(12) Marjon, K.; Cameron, M. J.; Quang, P.; Clasquin, M. F.; Mandley, E.; Kunii, K.; McVay, M.; Choe, S.; Kernytsky, A.; Gross, S.; Konteatis, Z.; Murtie, J.; Blake, M. L.; Travins, J.; Dorsch, M.; Biller, S. A.; Marks, K. M. MTAP deletions in cancer create vulnerability to targeting of the MAT2A/PRMT5/RIOK1 Axis. *Cell Rep.* **2016**, *15* (3), 574−587.
(13) Mavrakis, K. J.; McDonald, E. R., 3rd; Schlabach, M. R.; Billy, E.; Hoffman, G. R.; deWeck, A.; Ruddy, D. A.; Venkatesan, K.; Yu, J.; McAllister, G.; Stump, M.; deBeaumont, R.; Ho, S.; Yue, Y.; Liu, Y.; Yan-Neale, Y.; Yang, G.; Lin, F.; Yin, H.; Gao, H.; Kipp, D. R.; Zhao, S.; McNamara, J. T.; Sprague, E. R.; Zheng, B.; Lin, Y.; Cho, Y. S.; Gu, J.; Crawford, K.; Ciccone, D.; Vitari, A. C.; Lai, A.; Capka, V.; Hurov, K.; Porter, J. A.; Tallarico, J.; Mickanin, C.; Lees, E.; Pagliarini, R.; Keen, N.; Schmelzle, T.; Hofmann, F.; Stegmeier, F.; Sellers, W. R. Disordered methionine metabolism in MTAP/CDKN2A-deleted cancers leads to dependence on PRMT5. *Science* **2016**, *351* (6278), 1208−1213.
(14) Duncan, K. W.; Chesworth, R.; Boriack-Sjodin, P. A.; Munchhof, M. J.; Jin, L. PRMT5 inhibitors and uses thereof. U.S. Patent US8,993,555, March 31, 2015.
(15) Brehmer, D.; Beke, L.; Wu, T.; Millar, H. J.; Moy, C.; Sun, W.; Mannens, G.; Pande, V.; Boeckx, A.; van Heerde, E.; Nys, T.; Gustin, E. M.; Verbist, B.; Zhou, L.; Fan, Y.; Bhargava, V.; Safabakhsh, P.; Vinken, P.; Verhulst, T.; Gilbert, A.; Rai, S.; Graubert, T. A.; Pastore, F.; Fiore, D.; Gu, J.; Johnson, A.; Philippar, U.; Morschhauser, B.; Walker, D.; De Lange, D.; Keersmaekers, V.; Viellevoye, M.; Diels, G.; Schepens, W.; Thuring, J. W.; Meerpoel, L.; Packman, K.; Lorenzi, M. V.; Laquerre, S. Discovery and pharmacological characterization of JNJ-64619178, a novel small molecule inhibitor of PRMT5 with potent anti-tumor activity. *Mol. Cancer Ther.* **2021**, *20* (12), 2317−2328.
(16) Tatlock, J. H.; McAlpine, I. J.; Tran-Dube, M. B.; Rui, E. Y.; Wythes, M. J.; Kumpf, R. A.; McTigue, M. A.; Patman, R. Substituted carbonucleoside derivatives useful as anticancer agents. U.S. Patent US10,220,037, March 05, 2019.
(17) A Study of PRT543 in Participants with Advanced Solid Tumors and Hematologic Malignancies. *ClinicalTrials.gov*; U.S. National Library of Medicine, U.S. National Institutes of Health: Bethesda, MD, 2021; NCT03886831, https://clinicaltrials.gov/ct2/show/NCT03886831?term=NCT03886831&draw=2&rank=1 (accessed 2021-11-05).
(18) A Study of PRT811 in Participants with Advanced Solid Tumors, CNS Lymphoma and Gliomas. *ClinicalTrials.gov*; U.S. National Library of Medicine, U.S. National Institutes of Health: Bethesda, MD, 2021; NCT04089449, https://clinicaltrials.gov/ct2/show/NCT04089449?term=NCT04089449&draw=2&rank=1 (accessed 2021-11-05).
(19) Chan-Penebre, E.; Kuplast, K. G.; Majer, C. R.; Boriack-Sjodin, P. A.; Wigle, T. J.; Johnston, L. D.; Rioux, N.; Munchhof, M. J.; Jin, L.; Jacques, S. L.; West, K. A.; Lingaraj, T.; Stickland, K.; Ribich, S. A.; Raimondi, A.; Scott, M. P.; Waters, N. J.; Pollock, R. M.; Smith, J. J.; Barbash, O.; Pappalardi, M.; Ho, T. F.; Nurse, K.; Oza, K. P.; Gallagher, K. T.; Kruger, R.; Moyer, M. P.; Copeland, R. A.; Chesworth, R.; Duncan, K. W. A selective inhibitor of PRMT5 with in vivo and in vitro potency in MCL models. *Nat. Chem. Biol.* **2015**, *11* (6), 432−437.
(20) Duncan, K. W.; Rioux, N.; Boriack-Sjodin, P. A.; Munchhof, M. J.; Reiter, L. A.; Majer, C. R.; Jin, L.; Johnston, L. D.; Chan-Penebre, E.; Kuplast, K. G.; Porter Scott, M.; Pollock, R. M.; Waters, N. J.; Smith, J. J.; Moyer, M. P.; Copeland, R. A.; Chesworth, R. Structure and property guided design in the identification of PRMT5 tool compound EPZ015666. *ACS Med. Chem. Lett.* **2016**, *7* (2), 162−166.
(21) Bonday, Z. Q.; Cortez, G. S.; Grogan, M. J.; Antonysamy, S.; Weichert, K.; Bocchinfuso, W. P.; Li, F.; Kennedy, S.; Li, B.; Mader, M. M.; Arrowsmith, C. H.; Brown, P. J.; Eram, M. S.; Szewczyk, M. M.; Barsyte-Lovejoy, D.; Vedadi, M.; Guccione, E.; Campbell, R. M. LLY-283, a potent and selective inhibitor of arginine methyltransferase 5, PRMT5, with antitumor activity. *ACS Med. Chem. Lett.* **2018**, *9* (7), 612−617.
(22) Rodon Ahnert, J.; Perez, C. A.; Wong, K. M.; Maitland, M. L.; Tsai, F.; Berlin, J.; Liao, K. H.; Wang, I.-M.; Markovtsova, L.; Jacobs, I. A.; Cavazos, N.; Li, M.; Tolcher, A. W. PF-06939999, a potent and selective PRMT5 inhibitor, in patients with advanced or metastatic solid tumors: a phase 1 dose escalation study. *J. Clin. Oncol.* **2021**, *39*, 3019.
(23) Siu, L. L.; Rasco, D. W.; Vinay, S. P.; Romano, P. M.; Menis, J.; Opdam, F. L.; Heinhuis, K. M.; Egger, J. L.; Gorman, S. A.; Parasrampuria, R.; Wang, K.; Kremer, B. E.; Gounder, M. M. METEOR-1: a phase I study of GSK3326595, a first-in-class protein arginine methyltransferase 5 (PRMT5) inhibitor, in advanced solid tumours. *Ann. Oncol.* **2019**, *30*, v159.
(24) Cottrell, K. M.; Maxwell, J. P.; Whittington, D. A. Preparation of substituted *N*-(2-hydroxy-2-(1,2,3,4-tetrahydroisoquinolin-3-yl)-ethyl) amides for treating MTAP-deficient and/or MTA-accumulating diseases. World Patent WO/2021086879, May 06, 2021.
(25) Allen, J. R.; Amegadzie, A.; Beylkin, D. J.; Booker, S.; Bourbeau, M. P.; Butler, J. R.; Frohn, M. J.; Glad, S. O. S.; Husemoen, B. W.; Kaller, M. R.; Butler, J. R.; Frohn, M. J.; Glad, S. O. S.; Husemoen, B. W.; Kaller, M. R.; Kohn, T. J.; Lanman, B. A.; Li, K.; Liu, Q.; Lopez, P.; Ma, V. V.; Manoni, F.; Medina, J.; Minatti, A. E.; Peiro Cadahia, J.; Pettus, L.; Pickrell, A. J.; Sarvary, I.; Tamayo, N. A.; Vestergaard, M. Preparation of naphthyridinecarboxamide and quinolinecarboxamide compounds as PRMT5 inhibitors. World Patent WO/2021163344, August 19, 2021.
(26) Malik, R.; Park, P. K.; Barbieri, C. M.; Blat, Y.; Sheriff, S.; Weigelt, C. A.; Kopcho, L.; Celiktas, M.; Ruzanov, M.; Naglich, J. G.; Price, D. A.; Harner, M.; O'Malley, K. M.; Deng, J.; Schmitz, W.; Li, G.; Ruan, Z.; Qin, L.; Duke, G. J.; Rodrigo, I.; Witmer, M. R.; Harden, D. G.; Demes, S.; Arey, B. J.; Soars, M.; Fink, B. E.; Gavai, A. V.; Vite, G. D.; Voliva, C. F. Abstract 1140: A novel MTA non-competitive PRMT5 inhibitor. In *Experimental and Molecular Therapeutics*; American Association for Cancer Research, 2021.
(27) Baker, M. Fragment-based lead discovery grows up. *Nat. Rev. Drug Discovery* **2013**, *12* (1), 5−7.
(28) Carr, R. A.; Congreve, M.; Murray, C. W.; Rees, D. C. Fragment-based lead discovery: leads by design. *Drug Discovery Today* **2005**, *10* (14), 987−992.
(29) Linke, P.; Amaning, K.; Maschberger, M.; Vallee, F.; Steier, V.; Baaske, P.; Duhr, S.; Breitsprecher, D.; Rak, A. An automated microscale thermophoresis screening approach for fragment-based lead discovery. *J. Biomol. Screen.* **2016**, *21* (4), 414−421.
(30) Wartchow, C. A.; Podlaski, F.; Li, S.; Rowan, K.; Zhang, X.; Mark, D.; Huang, K. S. Biosensor-based small molecule fragment screening with biolayer interferometry. *J. Comput. Aided Mol. Des.* **2011**, *25* (7), 669−676.

https://doi.org/10.1021/acs.jmedchem.1c01900
J. Med. Chem. XXXX, XXX, XXX−XXX

(31) Osborne, J.; Panova, S.; Rapti, M.; Urushima, T.; Jhoti, H. Fragments: where are we now? *Biochem. Soc. Trans.* **2020**, *48* (1), 271−280.
(32) Edfeldt, F. N.; Folmer, R. H.; Breeze, A. L. Fragment screening to predict druggability (ligandability) and lead discovery success. *Drug Discovery Today* **2011**, *16* (7−8), 284−287.
(33) Ho, M. C.; Wilczek, C.; Bonanno, J. B.; Xing, L.; Seznec, J.; Matsui, T.; Carter, L. G.; Onikubo, T.; Kumar, P. R.; Chan, M. K.; Brenowitz, M.; Cheng, R. H.; Reimer, U.; Almo, S. C.; Shechter, D. Structure of the arginine methyltransferase PRMT5-MEP50 reveals a mechanism for substrate specificity. *PLoS One* **2013**, *8* (2), e57008.
(34) Morana, A.; Di Lernia, I.; Carteni, M.; De Rosa, R.; De Rosa, M. Synthesis and characterisation of a new class of stable S-adenosyl-L-methionine salts. *Int. J. Pharm.* **2000**, *194* (1), 61−68.
(35) *Molecular Operating Environment (MOE)*;Chemical Computing Group, 2020.
(36) Hughes, J. D.; Blagg, J.; Price, D. A.; Bailey, S.; Decrescenzo, G. A.; Devraj, R. V.; Ellsworth, E.; Fobian, Y. M.; Gibbs, M. E.; Gilles, R. W.; Greene, N.; Huang, E.; Krieger-Burke, T.; Loesel, J.; Wager, T.; Whiteley, L.; Zhang, Y. Physiochemical drug properties associated with in vivo toxicological outcomes. *Bioorg. Med. Chem. Lett.* **2008**, *18* (17), 4872−4875.
(37) Johnson, T. W.; Dress, K. R.; Edwards, M. Using the golden triangle to optimize clearance and oral absorption. *Bioorg. Med. Chem. Lett.* **2009**, *19* (19), 5560−5564.
(38) Leeson, P. D.; Springthorpe, B. The influence of drug-like concepts on decision-making in medicinal chemistry. *Nat. Rev. Drug Discovery* **2007**, *6* (11), 881−890.
(39) Waring, M. J. Defining optimum lipophilicity and molecular weight ranges for drug candidates-Molecular weight dependent lower logD limits based on permeability. *Bioorg. Med. Chem. Lett.* **2009**, *19* (10), 2844−2851.
(40) *Spartan'18*; Wavefunction, Inc., 2019.
(41) LaPlante, S. R.; Edwards, P. J.; Fader, L. D.; Jakalian, A.; Hucke, O. Revealing atropisomer axial chirality in drug discovery. *ChemMedChem.* **2011**, *6* (3), 505−513.
(42) LaPlante, S. R.; Fader, L. D.; Fandrick, K. R.; Fandrick, D. R.; Hucke, O.; Kemper, R.; Miller, S. P. F.; Edwards, P. J. Assessing atropisomer axial chirality in drug discovery and development. *J. Med. Chem.* **2011**, *54* (20), 7005−7022.
(43) Eliel, E. L.; Wilen, S. H. *Stereochemistry of Organic Compounds*, 1st ed.; Eliel, E. L., Wilen, S. H., Eds.; John Wiley & Sons: Nashville, TN, 1994.
(44) Quinn, J. G.; Pitts, K. E.; Steffek, M.; Mulvihill, M. M. Determination of affinity and residence time of potent drug-target complexes by label-free biosensing. *J. Med. Chem.* **2018**, *61* (12), 5154−5161.
(45) Bobinski, T. P.; Smith, C. R.; Marx, M. A.; Ketcham, J. M.; Burns, A. C.; Lawson, J. D.; Kulyk, S.; Kuehler, J.; Ivetac, A. MTA-cooperative PRMT5 inhibitors. WO Patent WO/2021050915, March 18, 2021.
(46) Clarke, S. I.; Kasum, B.; Prager, R. H.; War, A. D. Central nervous system active compounds. XII. The synthesis and properties of 3-dimethylaminomethylene phthalides. *Aust. J. Chem.* **1983**, *36* (12), 2483.
(47) Singh, J.; Sardana, V.; Jain, P. C.; Anand, N. Lactam acetals: part X−Synthesis of cyclic enaminones and fused heterocyclic systems. *Indian J. Chem., Section B* **1983**, *22B* (11), 1083−1086.
(48) Barl, N. M.; Sansiaume-Dagousset, E.; Monzon, G.; Wagner, A. J.; Knochel, P. Preparation and reactions of heteroarylmethylzinc reagents. *Org. Lett.* **2014**, *16* (9), 2422−2425.
(49) Sanchez-Vega, F.; Mina, M.; Armenia, J.; Chatila, W. K.; Luna, A.; La, K. C.; Dimitriadoy, S.; Liu, D. L.; Kantheti, H. S.; Saghafinia, S.; Chakravarty, D.; Daian, F.; Gao, Q.; Bailey, M. H.; Liang, W. W.; Foltz, S. M.; Shmulevich, I.; Ding, L.; Heins, Z.; Ochoa, A.; Gross, B.; Gao, J.; Zhang, H.; Kundra, R.; Kandoth, C.; Bahceci, I.; Dervishi, L.; Dogrusoz, U.; Zhou, W.; Shen, H.; Laird, P. W.; Way, G. P.; Greene, C. S.; Liang, H.; Xiao, Y.; Wang, C.; Iavarone, A.; Berger, A. H.; Bivona, T. G.; Lazar, A. J.; Hammer, G. D.; Giordano, T.; Kwong, L. N.; McArthur, G.; Huang, C.; Tward, A. D.; Frederick, M. J.; McCormick, F.; Meyerson, M. N.; Van Allen, E. M.; Cherniack, A. D.; Ciriello, G.; Sander, C.; Schultz, N.; et al. Oncogenic signaling pathways in the cancer genome atlas. *Cell* **2018**, *173* (2), 321−337.e10.

https://doi.org/10.1021/acs.jmedchem.1c01900
J. Med. Chem. XXXX, XXX, XXX−XXX